University of Alberta

Restructuring of soot particles by surface coatings

by

Rouzbeh Ghazi

A thesis submitted to the Faculty of Graduate Studies and Research in partial fulfillment of the requirements for the degree of

Master of Science
Department of Mechanical Engineering

Fall 2012
Edmonton, Alberta

Abstract

The size distribution, volatile mass fraction, effective density, mass concentration and mass-mobility exponent of particles from an inverted burner and a McKenna burner were measured with a Differential Mobility Analyzer (DMA) and a Centrifugal Particle Mass Analyzer (CPMA). Based on these properties a recommendation was made to choose an appropriate burner and flow settings for an investigation on the effect of coating thickness on the morphology of soot particles. Oleic acid and dioctyl sebacate (DOS) was used as a coating material in a wide range of coating thicknesses. It was shown that as the coating mass increases the degree of collapsing increases. A model is presented to predict the change in mobility diameter as a function of coating mass ratio. The change of effective density and shape factor of soot particles in coating/denuding process is also reported.

Acknowledgments

I would like to express my deep appreciation to my supervisor Dr. Jason Olfert. Thank you for your help and support throughout this research. I could not have asked for a better supervisor.

I would like to thank the Mechanical Engineering workshop staff, in particular: Michael Andrech, Roger Marchand, and Dave Waege who helped me in manufacturing and building of the experiment setup. I thank Rick Conrad for his help in setting up electrical equipment, troubleshooting the electrical devices. I would also thank Tyler Johnson for his generous help in the CPMA maintenance. I also appreciate the patience of Alireza Vail, Mona Abdolrazaghi, Mathew Bussiere and Alex Schramm to tolerate the CPMA noise. I would also like to take this opportunity to thank colleagues and friends who have kept me happy over these years.

Finally, I could not have done this without the support and encouragement of my family. My sincere appreciation is given to my parent for their encouragement and continues support. Likewise, words are insufficient to express my love and gratitude to my wife, Afsaneh.

Table of contents

List of Tables

List of Figures

List of Nomenclature

C_c ..... slip correction factor

D_f ..... fractal dimension

D_{fm} ..... mass-mobility exponent

d_0 ..... mobility diameter of initial soot particles (nm)

$d_{denuded}$ ..... mobility diameter after the coating/denuding process(nm)

d_m ..... electrical mobility diameter (nm)

d_{me} ..... mass equivalent diameter (nm)

d_{ve} ..... volume equivalent diameter (nm)

e ..... electronic charge (1.602×10^{-19} C)

E ..... electric field between to coaxial cylinders (V/m)

m_p ..... mass of the particle (fg)

N ..... number of primary particles

Kn ..... Knudsen number

Q_{sh} ..... flow rate of sheath flow (lpm)

Q_e ..... flow rate of excess flow (lpm)

R_g ..... radius of gyration of the aggregate (nm)

r_1 ..... inner radius of the cylinders (for DMA or CPMA) (m)

r_2 ..... outer radius of the cylinders (for DMA or CPMA)(m)

V_c ..... voltage at which the transfer function is maximum (V)

V_m ..... material volume (nm^3)

V_p ..... particle volume (nm^3)

V ..... voltage between the cylinder and inner rod (V)

Z ..... electrical mobility ($m^2/V\bullet s$)

β ..... mechanical mobility ($m/N\bullet s$)

χ ..... shape factor

Φ ..... equivalence ratio

λ ..... mean free path (nm) / dimensionless constant of the CPMA (μm)

ρ_{eff} ..... effective density (kg/m^3)

ρ_m .....material density (kg/m^3)

ρ_p .....particle density (kg/m^3)

Ω .....transfer function

ω_c .....angular velocity of CPMA (rad/s)

Abbreviations

CPC.....condensation particle counter

CPMA.....centrifugal particle mass analyzer

DMA.....differential mobility analyzer

DOS.....dioctyl sebacate

Chapter 1: Introduction

1.1 Introduction

The research on soot particles has increased dramatically over the last few decades. This could be because of their profound impacts on precipitation, climate change, visibility and human health. Soot particles form in many combustion systems though usually it has negative effects. Soot formation depends on fuel, air to fuel ratio, temperature and pressure of the flame (Böhm et al., 1988).

1.2 Soot impacts

Soot participles can have some negative effects on the climate by scattering and absorbing solar radiation. Solar radiation can be altered when it propagates through the atmosphere. Light can be scattered or absorbed by aerosol particles and the optical properties of aerosol depend on the chemical composition, the size, the morphology, and the coating (Kokhanovsky, 2008). The scattering or absorbing process causes the intensity of a light beam to decrease as it passes through an aerosol medium. Among aerosol particles, black carbon is most responsible for light absorption (Horvath, 1993). The total light scattering in all directions and absorption is called extinction. The extinction causes the intensity of the sunlight to decrease when it reaches the earth. Absorption causes an increase in the heat input to the atmosphere and hence increasing in temperature. However, because of the effect of light scattering, part of the sunlight is reflected back into the space, which causes a decrease in the temperature. The net cooling

or warming effect depends on the single scattering albedo. Consequently, changing properties of an aerosol can change the heat balance of the atmosphere and cause climate change.

The ratio of the scattering coefficient to the extinction coefficient is called the single scattering albedo. The single scattering albedo indicates the relative importance of absorption and scattering and ranges from 0 to 1. It is generally accepted that aerosols with a single scattering albedo less than 0.85 cause an increase in the temperature and greater than 0.85 (more transparent) generally cause a decrease in the temperature (Takemura and Nakajima, 2002). The single scattering albedo of soot particles will increase as the particles age and acquire coatings (Gao et al., 2007). For fresh soot the absorption coefficient is greater than the scattering coefficient, therefore the single scattering albedo can be as small as 0.09. However Xue et al. (2009) reported that the single scattering albedo increased from 0.09 to 0.24 by coating the soot with glutaric acid.

Deposition of soot on snow enhances sunlight absorption which can lead to melting (Ramanathan and Carmichael, 2008). Soot particles can be considered as the second largest contribution to the direct positive radiative forcing (RF) of Earth's climate. The best estimate of radiative forcing due to soot particles is 0.9 W/m^2, with a uncertainty range of 0.4 to 1.2 W/m^2 (Ramanathan and Carmichael, 2008). This value is about 55% of carbon dioxide (1.66±0.17 W/m^2) and greater than methane (0.48±0.05 W/m^2) which are respectively the most important and the second most important green house gasses. Although greenhouse gases can be assessed by use of the global warming potential (GWP), deriving a GWP for soot

particles has some problems. This is due the fact that the absorption of soot particles can change more than two times depending on their sources and their aging process (Chameides and Bergin, 2002).

Considering the soot has major negative role in global radiative forcing, and a much shorter lifetime compared with CO_2, decreasing soot can decrease the effects of global warming trends in the short term (Ramanathan and Carmichael, 2008).

Soot particles also can indirectly affect climate by changing the properties of clouds such as their lifetime. Soot particles can act as cloud condensation nuclei (CCN). Increasing the concentration of soot particles (or more generally, aerosol particles) can increase the concentration of CCN, so more cloud droplets are created, and thus the cloud droplet is smaller for a fixed amount of cloud liquid water content. This leads to an increase in cloud reflectivity and brighter clouds which is called "cloud albedo effect" (Remer et al., 2007).

Visibility can be defined as a clarity with which distant objects can be seen (Hinds, 1999), and visual range which is the distance at which objects are barely discernible. Absorption and scattering effects of atmospheric particles such as soot can directly affect visibility. Eidels-Dubovoi (2002) measured visible light absorption and scattering with an aethalometer and an integrating nephelometer at two different sites in the Mexico City. His results show that the average visibility in the downtown area was 20.9 km, which was 9.4 km lower than the suburban area.

It has been known for a long time that air pollution, including soot, may have a negative effect on human health. By the 1980s, the link between very high concentrations of particular matter (PM) air pollution and cardiopulmonary disease was suggested (Pope III and Dockery, 2006). Depending on the size of the particles, they can deposit at different parts of the respiratory tract. For example PM_{10} (aerodynamic diameter smaller than 10 μm) particles deposit generally in the upper respiratory tract but fine (smaller than 1μm) and ultra fine (smaller than 100nm) particles can reach lung alveoli. Studies suggest that ultra fine and fine particles are more harmful than coarse particles (Kampa and Castanas, 2008). These harmful effects are suggested to be nausea, difficulty in breathing or even cancer, early death and cardiopulmonary mortality. Air pollution may affect the respiratory system, cardiovascular system, nervous system, urinary system and digestive system (Kampa and Castanas, 2008). Schwartz et al. (2005) results show there is relation between particle concentration and heart rate variability (HRV), a risk factor for sudden death. Although effects of short-term exposures are important, several studies suggest that long-term exposure may be more important in terms of overall public health (Pope III et al., 2002).

Although most concentration of soot produced outdoors, humans spend most of their time indoors and particle concentrations can be relatively high indoors. For example Wallace et al. (2011) measured ultrafine particles in 50 homes in Edmonton. Their results show that the indoor number concentration was 40% higher than outdoor concentration. Therefore, soot may have a relatively small

effect on human health in terms of PM exposure. The major source of indoor particles was cooking.

1.3 Soot characteristics

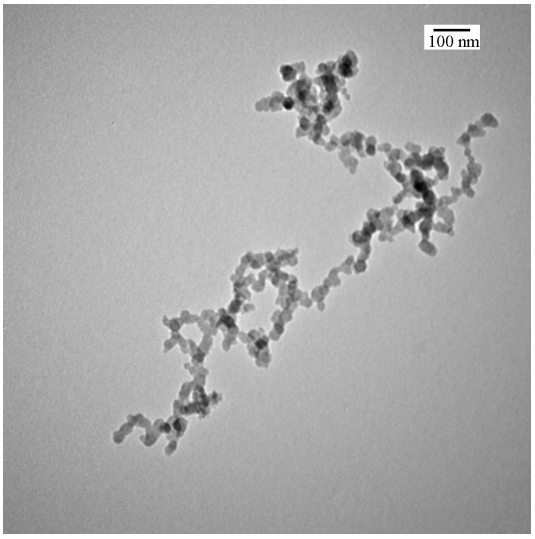

(a)

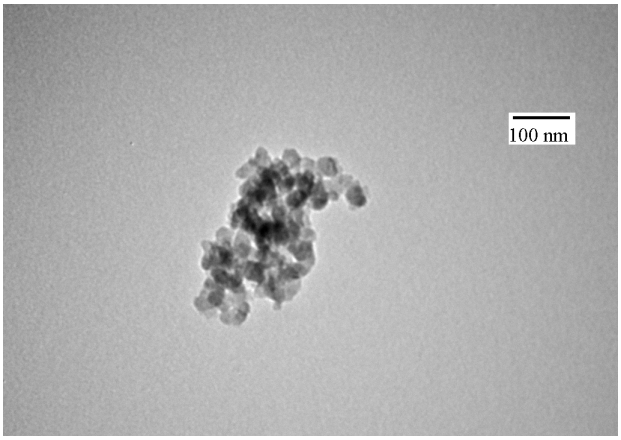

(b)

Figure 1.1. TEM images of agglomerates and their primary particles

Soot particles, which are also called black carbon (BC), have complex geometry and physical properties. Soot particles are agglomerates of small individual particles, called spherules or primary particles which are usually about 15-30 nm in diameter (Slowik et al., 2004). Although the soot particles can have different size and morphology, the primary particles within a particle are usually consistent (Seinfeld and Pandis, 2006). Figure 1.1 shows the Transmission electron microscopy (TEM) image of agglomerates and their primary particles. In Fig 1.1(a) the soot particle has a morphology that is chain-like and Fig 1.1(b) shows a more compact soot particle, having a morphology closer to a sphere. The size of these aggregates change and can be up to several micrometers.

Although the fresh soot is hydrophobic, during their lifetime in the atmosphere, which is approximately 1±1 weeks (McMeeking et al., 2011), they undergo an aging process and become hydrophilic. Sulfates or other organic materials can condense on these hydrophilic particles and change its optical properties such as absorption or scattering. They also can affect the morphology of the chain-like soot particles and cause them to restructure to a more compact shape (Xue et al., 2009b). The coating of soot particles in the atmosphere may have a significant, complex, effect on the optical properties of the particles. On one hand the coating would work like a magnifier and increase the absorption and on the other hand by decreasing the projected area it decreases the absorbing. So the total effect of aging soot particles in atmosphere is complex and highly uncertain.

1.4 Outline of the thesis

This thesis includes five chapters. An introduction to soot particles, their formation, characteristic and impact were presented in the first chapter. The apparatus and the experimental setup are explained in detail in the second chapter. This study consists of two main parts which are presented in the third and fourth chapter. In the third chapter the size distribution, volatile mass fraction, effective density, mass concentration and mass-mobility exponent of particles from an inverted burner and a McKenna burner were studied and some data provided to choose an appropriate burner for particular applications. Based on the results of this chapter, since the generated soot particles from the inverted burner does not have any coating on them, the inverted burner was chose for studied effects of coating on soot particles. Studying particle morphology is a significant subject because as mention before the optical properties of soot depends on its morphology. In the fourth chapter the effect of coating thickness on the morphology of soot particles is investigated. A model is also suggested predicting the change in mobility diameter after the coating/denuding process in the fourth chapter. In the last chapter, chapter five, conclusions and recommendations for further studies are provided.

1.5 References

Böhm, H., Hesse, D., Jander, H., Lüers, B., Pietscher, J., Wagner, H.G.G., Weiss, M., 1988. The influence of pressure and temperature on soot formation in premixed flames. *22nd International Symposium on Combustion. The Combustion Institute* 403-411.

Chameides, W.L., Bergin, M., 2002. Perspectives climate change- Soot takes center stage. *Science* 297, 2214-5.

Eidels-Dubovoi, S., 2002. Aerosol impacts on visible light extinction in the atmosphere of Mexico City. *The Science of the Total Environment* 287, 213-20.

Gao, R.S., Schwarz, J.P., Kelly, K.K., Fahey, D.W., Watts, L. a., Thompson, T.L., Spackman, J.R., Slowik, J.G., Cross, E.S., Han, J.-H., Davidovits, P., Onasch, T.B., Worsnop, D.R., 2007. A novel method for estimating light-scattering properties of soot aerosols using a modified single-particle soot photometer. *Aerosol Science and Technology* 41, 125-135.

Hinds, W.C., 1999. Aerosol technology—properties, behavior, and measurement of airborne particles., 2nd ed. John Wiley & Sons, New York,

Horvath, H., 1993. Atmospheric light absorption-A review. *Atmospheric Environment* 27A, 293-317.

Kampa, M., Castanas, E., 2008. Human health effects of air pollution. *Environmental pollution*,151, 362-7.

Kokhanovsky, A.A., 2008. Aerosol optics light absorption and scattering by particles in the atmosphere, Book. Springer-Praxis, Berlin.

McMeeking, G.R., Good, N., Petters, M.D., McFiggans, G., Coe, H., 2011. Influences on the fraction of hydrophobic and hydrophilic black carbon in the atmosphere. *Atmospheric Chemistry and Physics II*, 5099-5112.

Pope III, C.A., Burnett, R.T., Thun, M.J., Calle, E.E., Krewski, D., Thurston, G.D., 2002. Lung cancer, cardiopulmonary mortality, and long-term exposure to fine particulate air pollution. *Journal of the American Medical Association* 287, 1132-1141.

Pope III, C.A., Dockery, D.W., 2006. Health Effects of Fine Particulate Air Pollution - Lines that Connect. *Journal of the Air & Waste Management Association* 56, 709-742.

Ramanathan, V., Carmichael, G., 2008. Global and regional climate changes due to black carbon. *Nature Geoscience* 221-227.

Remer, A.L.A., Gsfc, N., Chin, M., Decola, P., Hq, N., Fein-, G., Kahn, R.A., Quinn, P.K., Rind, D., Giss, N., Schwartz, S.E., Bnl, D.O.E., Streets, D.G., Anl, D.O.E., Yu, H., Umbc, N.G., 2007. Atmospheric aerosol properties and climate impacts. *The U.S. Climate Change Science Program*, Executive Summary.

Schwartz, J., Litonjua, a, Suh, H., Verrier, M., Zanobetti, a, Syring, M., Nearing, B., Verrier, R., Stone, P., MacCallum, G., Speizer, F.E., Gold, D.R., 2005. Traffic related pollution and heart rate variability in a panel of elderly subjects. *Thorax* 60, 455-61.

Seinfeld, J.H., Pandis, S.N., 2006. Atmospheric chemistry and physics. John Wiley & Sons, Inc, New York.

Slowik, J.G., Stainken, K., Davidovits, P., Williams, L., Jayne, J., Kolb, C., Worsnop, D., Rudich, Y., DeCarlo, P., Jimenez, J., 2004. Particle morphology and density characterization by combined mobility and aerodynamic diameter measurements. part 2: Application to combustion-generated soot aerosols as a function of fuel equivalence ratio. *Aerosol Science and Technology* 38, 1206-1222.

Takemura, T., Nakajima, T., 2002. Single-scattering albedo and radiative forcing of various aerosol species with a global three-dimensional model. *Journal of Climate* 15, 333-352.

Wallace, L., Wheeler, A Warren Kindzierski; Marie-Ève Héroux, 2011, Indoor-outdoor ultrafine particles in 50 homes in Edmonton, Canada, Indoor air conference, June 5-11, Austin, Texas

Xue, H., Khalizov, A.F., Wang, L., Zheng, J., Zhang, R., 2009a. Effects of dicarboxylic acid coating on the optical properties of soot. *Physical Chemistry Chemical Physics* 11, 7869-7875.

Xue, H., Khalizov, A.F., Wang, L., Zheng, J., Zhang, R., 2009b. Effects of coating of dicarboxylic acids on the mass-mobility relationship of soot particles. *Environmental Science & Technology* 43, 2787-92.

Chapter 2: Particle morphology and principles

2.1 Particle morphology and principles

In the following section some information about particle morphology and principles of aerosol science will be presented.

Equivalent diameters. For spherical particles[1] the universal accepted way of measuring the size is the diameter or radius. However, as it was shown in Fig 1.1 particles are not always a perfect sphere, they can be chain-like or have some void spaces. In these cases the relation between mass, density and volume and their measurement can be more complex. Therefore equivalent diameters (such as mobility equivalent diameter) or densities (such as effective density) should be introduced to define the properties of nonspherical particles. The first diameter can be define is the volume equivalent diameter, d_{ve}. The volume equivalent diameter is defined as the diameter of a spherical particle of the same volume as the particle under consideration (Kulkarni et al., 2011). According to the definition, the volume equivalent diameter of a sphere with internal voids is equal to the physical diameter. The concept of mass equivalent diameter (d_{me}) definition is similar to the volume equivalent diameter. The mass equivalent diameter is defined as the diameter of a nonporous spherical particle composed of the bulk particle material and has the same mass as the particle under consideration. The difference between these two diameters is for particles containing internal voids, because the mass equivalent diameter does not include internal voids.

[1] A spherical particle is defined here as a particle that is a perfect sphere, as opposed to a particle that is "sphere-like".

Density. Based on the volume and mass equivalent diameters, two different types of volume and density can be defined that consider or not consider internal voids. As expected the "material volume" and the "material density" does not take into the account the internal voids:

$$V_{\mathrm{m}} = \frac{\pi}{6} d_{\mathrm{me}}^3 \tag{2.1}$$

and

$$\rho_{\mathrm{m}} = \frac{m_{\mathrm{p}}}{V_{\mathrm{m}}} = \frac{m_{\mathrm{p}}}{\frac{\pi}{6} d_{\mathrm{me}}^3} \tag{2.2}$$

However, "particle volume" and "particle density" consider the internal voids:

$$V_{\mathrm{p}} = \frac{\pi}{6} d_{\mathrm{ve}}^3 = V_{\mathrm{m}} + V_{\mathrm{void}} \tag{2.3}$$

and

$$\rho_{\mathrm{p}} = \frac{m_{\mathrm{p}}}{V_{\mathrm{p}}} = \frac{m_{\mathrm{p}}}{\frac{\pi}{6} d_{\mathrm{ve}}^3} \tag{2.4}$$

In the case of no internal void then $\rho_{\mathrm{m}} = \rho_{\mathrm{p}}$, otherwise $\rho_{\mathrm{m}} > \rho_{\mathrm{p}}$.

Particle concentration. Depending on the application and the method of measurement, aerosol concentrations can be described in different ways such as number, mass, surface area, and volume concentration. Number concentration is analogous to density and the units of number concentration are m^{-3} (or cm^{-3}). The

total number concentration, in the urban atmosphere can range from 10^4 to 10^5 cm^{-3} depends on the pollution. The number concentrations of emission sources, such as diesel engine or burner can be 10^7 cm^{-3} or more (Kulkarni et al., 2011). As it will be discussed later in chapter 3, the maximum number concentrations for a McKenna burner and an inverted burner are $6.36\times10^7$and 1.7×10^7 cm^{-3}, respectively.

The most common units for mass concentration are $\mu g/m^3$and mg/m^3 and aerosol mass concentrations in the atmosphere can range from about 20 $\mu g/m^3$ to 200 $\mu g/m^3$ in polluted areas (Kulkarni et al., 2011). As it will be shown in chapter 3, the maximum mass concentration for the McKenna burner was about 123 $mg/m^3$and for the inverted burner it was about 42 mg/m^3.

Size and mass distributions. In the atmosphere and many applications, the aerosols are polydisperse and have a wide range of diameters which can be described by the size distribution. Depending on the application and the method of measurement the mass distribution also can be used, for example in pharmaceutical aerosols the most common way of presenting the data is in the mass distribution format (Finlay, 2001).

To present the size distribution the range of measurement are divided into different bins (each bin ranges from d_i to $d_i+\Delta d$) and the number of particles in each bin will be shown in the y axis. However, in this method the number concentration is depending on the bin width.

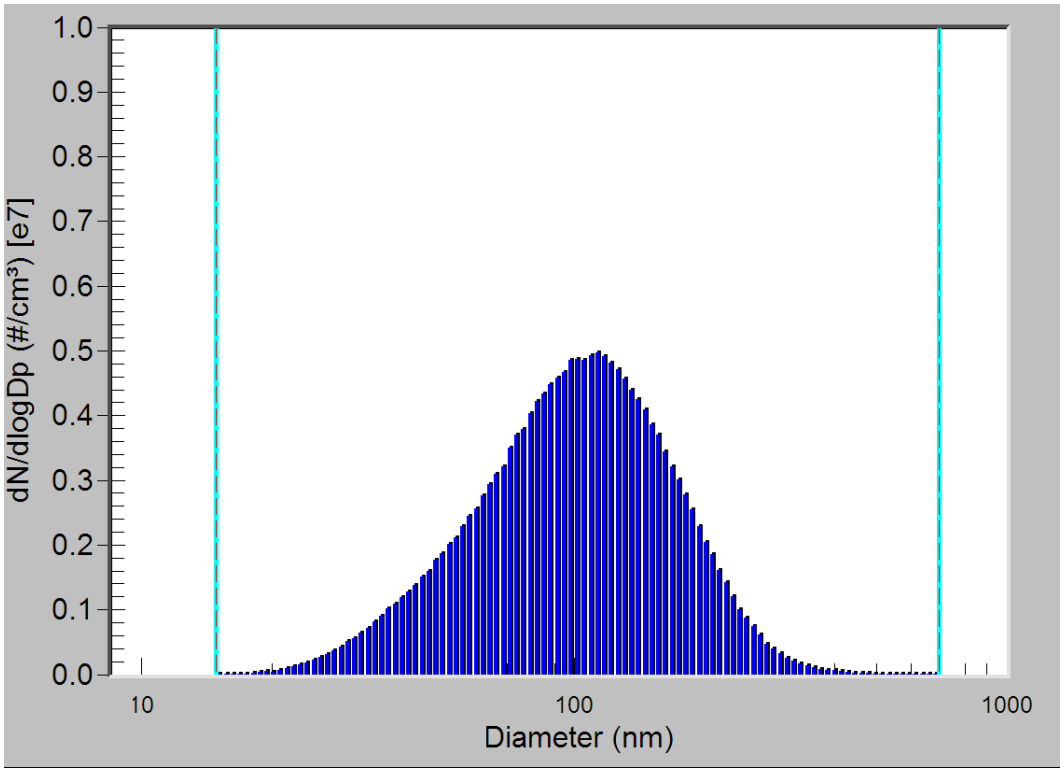

Figure 2.1. The sample size distribution from the McKenna burner

Thus the better way to present size distribution is to normalize the number of particles in each bin by the bin width. Usually the size distribution of aerosol follows a lognormal distribution, although there is no fundamental theoretical reason for that (Hinds, 1999). Figure 2.1 shows an example of a size distribution from the McKenna burner measured by the differential mobility analyzer (DMA) and the Condensation particle counters (CPC).

Drag force. Drag force is a force created by motion of a particle in a fluid and acting in the opposite direction of the particle motion relative to the fluid. The drag force is a function of several parameters including the flow regime. The flow regime can be determined by Knudsen number, *Kn*:

$$Kn = \frac{\lambda}{d_p / 2} \tag{2.5}$$

where λ is the mean free path and d_p is the diameter of the particle. When the particle is much bigger than the mean free path (Kn<<1) then the flow regime is continuum and when the particle is much smaller than mean free path (Kn>>1) the flow regime is free molecular flow. When Kn is between 0.4 to 20, the flow is called transition or slip flow regime (Kulkarni et al., 2011).

In the continuum regime one can show that the drag force on the sphere particle can be calculated by Stokes' law:

$$F_{\mathrm{d}} = 3\pi\eta v d_{\mathrm{p}} \tag{2.6}$$

where F_{d} is the drag force, η is dynamic viscosity of the gas and V is the relative velocity between the particle and the flow. As the Knudsen number increases the deviation from the above equation increases. In the transition regime it can be corrected by the slip correction factor, C_{c}, which can be calculated for particles less than 0.1 μm by (Hinds, 1999):

$$C_{\mathrm{c}} = 1 + \frac{\lambda}{d}[2.34 + 1.05\exp(-0.39\frac{\lambda}{d})] \tag{2.7}$$

Considering the correction factor the drag force on a sphere particle can be calculated by:

$$F_{\mathrm{d}} = \frac{3\pi\eta V d_{\mathrm{p}}}{C_{\mathrm{c}}(d_{\mathrm{p}})} \tag{2.8}$$

Dynamic shape factor. As mentioned before particles are not always a sphere, so the above equation should be modified for non-spherical particles. To correct the drag force for non-spherical particles the dynamic shape factor (χ) should be used. The dynamic shape factor is defined as the ratio of drag force on the particle to the drag force of a sphere particle having the same volume and velocity:

$$\chi = \frac{F_{\mathrm{d}} C_{\mathrm{c}}(d_{\mathrm{ve}})}{3\pi\eta V d_{\mathrm{ve}}} \tag{2.9}$$

The dynamic shape factor is usually equal or greater than one (Hinds, 1999). Although the value of the dynamic shape factor can depend on the flow regime, DeCarlo et al. (2004) results shows that for small values of $\chi < 2$, one can assume than the dynamic shape factor is constant at different flow regimes.

Fractal dimension and mass-mobility relation. Soot particles are fractal aggregates of primary particles. The mathematical relation of the size of the aggregate and the number of primary particles is:

$$N = k_0 (R_{\mathrm{g}} / a)^{D_{\mathrm{f}}} \tag{2.10}$$

where N is the number of primary particles, k_0 is proportionality constant, a is the radius of primary particles, D_{f} is the fractal dimension and R_{g} is the radius of gyration of the aggregate. D_{f} ranges from 1 for a linear chain to 3 for a sphere.

Assuming the same size for primary particles, and proportional relation between mass of the aggregate and number of primary particles, Park et al. (2003) showed that mass-mobility relationship can be used to estimate the fractal dimension:

$$m_{\mathrm{p}} = Cd_m^{D_{\mathrm{fm}}} \tag{2.11}$$

where m_{p} is mass of the particle, C is a constant and D_{fm} is called mass-mobility exponent. The mass-mobility exponent is not the fractal dimension although it is often presented in the literature as such (Kim et al., 2009). Park et al. (2004) reported the relation between the mass-mobility exponent and the fractal dimensionfor the diesel particles:

$$D_{\mathrm{f}} = \frac{D_{\mathrm{fm}}}{1.26} \tag{2.12}$$

2.2 References

DeCarlo, P., Slowik, J.G., Worsnop, D., Davidovits, P., Jimenez, J., 2004. Particle morphology and density characterization by combined mobility and aerodynamic diameter measurements. part 1: Theory. *Aerosol Science and Technology* 38, 1185-1205.

Finlay, W.H., 2001. The mechanics of inhaled pharmaceutical aerosols: An introduction. Academic Press, London.

Hinds, W.C., 1999. Aerosol technology—properties, behavior, and measurement of airborne particles., 2nd ed. John Wiley & Sons, New York, New York.

Kim, S.C., Wang, J., Emery, M.S., Shin, W.G., Mulholland, G.W., Pui, D.Y.H., 2009. Structural Property Effect of Nanoparticle Agglomerates on Particle Penetration through Fibrous Filter. *Aerosol Science and Technology* 43, 344-355.

Kulkarni, P., Baron, P.A., Willeke, K. (eds), 2011. Aerosol measurement: principles, techniques, and applications,, Third. ed. John Wiley & Sons, Inc., Hoboken, NJ.

Park, K., Cao, F., Kittelson, D.B., McMurry, P.H., 2003. Relationship between particle mass and mobility for diesel exhaust particles. *Environmental Science & Technology* 37, 577-83.

Park, K., Kittelson, D., McMurry, P., 2004. Structural Properties of Diesel Exhaust Particles Measured by Transmission Electron Microscopy (TEM): Relationships to Particle Mass and Mobility. *Aerosol Science & Technology* 38, 881-889.

Chapter 3: Apparatus and the experimental setup

In the following section each apparatus of the experiment including burners, ejectors, differential mobility analyzers, centrifugal particle mass analyzer, thermodenuder and coating chamber will be described.

3.1 Burners and ejectors

Two different types of burner were used in this study: a commercially available McKenna burner (Holthuis & Associated, Sebastopol, CA) and an inverted burner. In the following sections the details of both burners are presented.

3.1.1 McKenna burner and its ejector

A schematic and cross section view of McKenna burner is shown in Fig 3.1. Premixed fuel was provided to the burner from the "fuel inlet" tube. Ethylene (C_2H_4) was used as the fuel and it was supplied via a Cole-Parmer flow controller (model 32907-69). The flow rate of fuel was maintained between 1.114 to 2.09 SLPM which gave equivalence ratios of 2 to 3.75. The flow rate of air was held constant at 8 SLPM via a Cole-Parmer (model 32907-71) flow controller. A shroud of nitrogen gas, at flow rate of 35-45 SLPM, was used to shield the flame from the surrounding atmosphere. Cooling water was provided to the burner via a Cole-Parmer flow controller (model 32907-46) at flow rate of 400 mL/min at room temperature. The temperature difference between the inlet and the outlet of cooling water was about 5^{o}C.

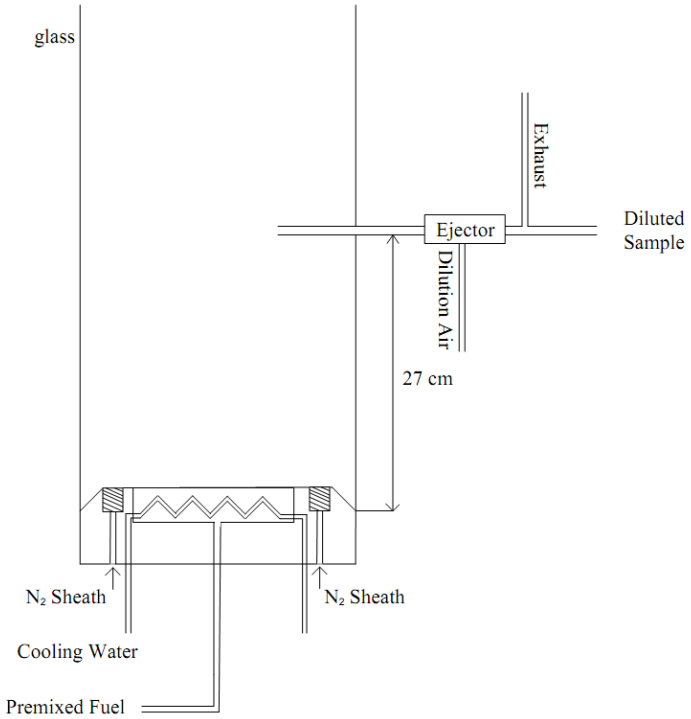

(a)

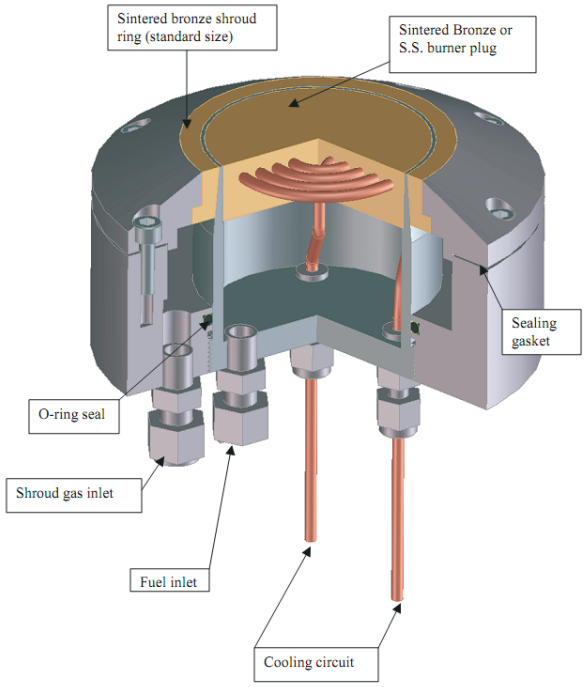

(b)

Figure 3.1. (a) Schematic and (b) cross section view of the McKenna burner (Source and permission: McKenna Flat Flame Burner manufacturer, Sebastopol, CA)

The flame was contained by a glass housing to minimize the effect of the surrounding atmosphere. The glass contains several holes at different heights for sampling at different heights. Except the hole at chosen height, the other holes are covered with aluminum tape. Depending on the height of the sampling hole the morphology and other properties of soot can change. At this study the sample was collected 27 cm above the burner and then diluted 15 times with an ejector dilutor. The design of ejector was bases on the Maricq et al. (2003) design. The schematic of the ejector is shown in Fig 3.2. Two tubes with different diameters were inserted to a Swagelok "tee". When the pressurized dilution air is provided to the "tee" the pressure drops, because the area (between two tubes) decreases (based on the Bernoulli equation). This decrease in pressure creates suction at the sample side. The dilution air was held between 15 to 20 SLPM via an Omega flow controller (model FMA-774-V).

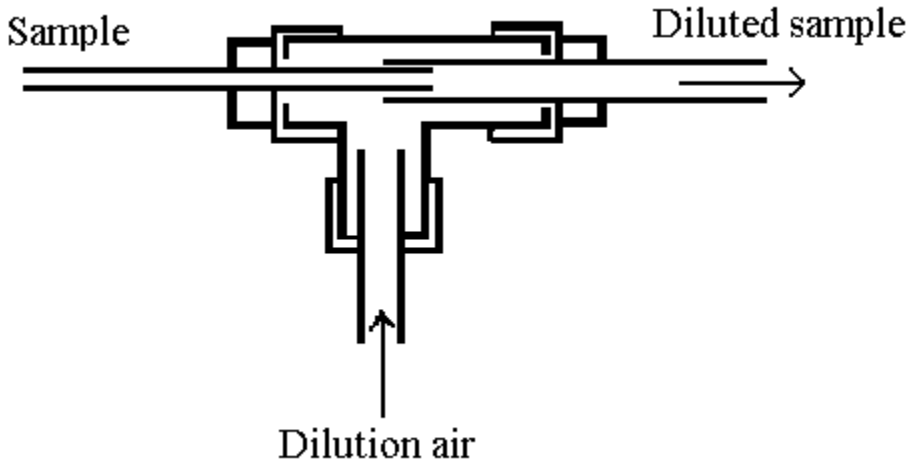

Figure 3.2. Schematic of ejector for McKenna burner

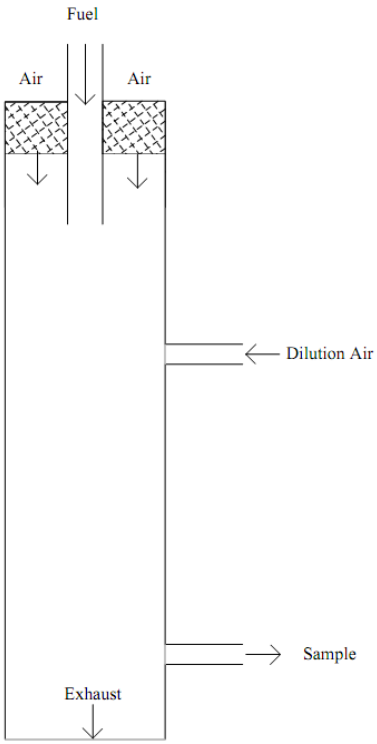

(a)

(b)

Figure 3.3. (a) Schematic and (b) a photo of the inverted burner

3.1.2 Inverted burner and its ejector

The inverted burner was based on design of Stipe et al.(2005) and Coderre et al., (2011).A schematic and a photo of the inverted burner are shown in Fig 3.3. The length of quartz tube was 48 cm and its outer diameter was 48 mm. Methane was supplied to the burner via mass flow controllers at flow rates of 1.03-1.26 provided equivalence ratios over the range of 0.55 to 0.69. The air was maintained at constant rate of 18 SLPM via Omega flow controller (model FMA-774-V). A flow straightener was used to make the air flow uniform. The sample was diluted at two stages. Primary dilution air, controlled by another mass flow controller (Omega, FMA-774-V), was injected into the exhaust at a flow rate of 29 to 45 SLPM to maintain the primary dilution ratio at 3.5. Soot particles were sampled 50 cm after the primary dilution by an ejector dilutor with a dilution ratio of 15. The diluter consists of two orifices with diameters of 0.014"and 0.017" (O'Keefe Controls Co., model K4-14-SS and K4-17-SS), which are inserted in a Swagelok "tee".

3.2 DMA

Two differential mobility analyzers (DMA; TSI, Model 3776) were used in this study. DMA is an instrument to measure the electrical mobility diameter, d_m. The electrical mobility diameter is defined as a diameter of a sphere with the same migration velocity as the considered particle in a constant electrical field. The DMA was first introduced by Knutson and Whitby (1975). DMA consists of coaxial stainless steel cylinder and inner rod.

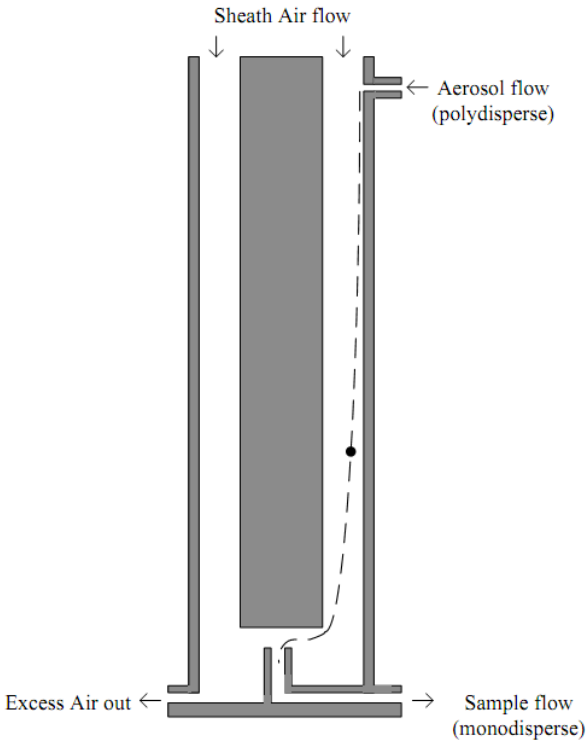

Figure 3.4. Schematic of DMA

The rod is connected to a high-voltage controller, which creates a uniform electrical field in the annular cavity between the rod and the cylinder. The electric field in the DMA can be calculated based on the electric field between to coaxial cylinders:

$$E = \frac{V}{r \ln(\frac{r_2}{r_1})} \tag{3.1}$$

where V is the voltage between the cylinder and inner rod, r_1 and r_2 are radius of the inner and outer electrodes, respectively and r is the radius of the location. The particle-free sheath flow goes through this annular cavity. Polydisperse soot particles pass through a Kr-85 bipolar charger to obtain a Boltzmann equilibrium charge distribution. The aerosol flow is injected from the outer side and since the

rod has negative polarity, positive particles are attracted to the rod:

$$F = qE \tag{3.2}$$

where q is the charge of the particle and E is the strength of the electrical field. The charge can be calculated by $q = ne$, where n is number of charges and e is unit charge ($e = 1.6 \times 10^{-19}$ C).Another force to the particle is drag force which can be calculated by modified Stokes' equation:

$$F_D = \frac{3\pi\mu V d_{\mathrm{p}}}{C_c(d_{\mathrm{p}})} \tag{3.3}$$

where μ is the viscosity of gas, V is velocity of particle, d_{p} is diameter of particle and C_c is slip correction factor. The slip correction is used to account for non-continuum effects for small particles. For most of the aerosol measurements equipment, one can assume that the particle reaches its terminal velocity instantly, and relaxation time is negligible. Thus the acceleration is zero and drag force and electrical force are equal, and velocity of the particle can be calculated by:

$$v = \frac{neEC_c(d_{\mathrm{p}})}{3\pi\mu d_{\mathrm{p}}} \tag{3.4}$$

or simply:

$$V = neE\beta \tag{3.5}$$

where β is mechanical mobility and equal to $\beta = \frac{C_c(d_{\mathrm{p}})}{3\pi\mu d_{\mathrm{p}}}$ and $ne\beta$ is called electrical mobility, Z, so:

$$Z = \frac{neC_c(d\mathrm{ve})}{3\pi\mu\chi d_{\mathrm{ve}}} \tag{3.6}$$

and

$$V = ZE \tag{3.7}$$

Thus the radial component of the velocity of particle can be calculated by:

$$V_r = \frac{Z_p V}{r\ln(\frac{r_2}{r_1})} \tag{3.8}$$

and its vertical component is equal to the velocity of flow at each radius, $u(r)$:

$$V_x = u(r) \tag{3.9}$$

Thus the particle trajectory can be described by these two above equations:

$$\frac{dr}{dx} = \frac{dr/dt}{dx/dt} = \frac{Z_{\mathrm{p}} V}{ru(r)\ln(\frac{r_2}{r_1})} \tag{3.10}$$

Consequently, at a set voltage of the rod only positively charged particles with a narrow range of mobility diameters can exit through the circumferential slit. From

the trajectories of the particles in the DMA, one can show that the electrical mobility of the particle entering at the middle of the incoming aerosol slit and exits at the middle of the classified aerosol outlet flow is (Z_p^*):

$$Z_p^* = \frac{(Q_{sh} + Q_e)\ln(\frac{r_2}{r_1})}{4\pi VL} \tag{3.11}$$

where Q_{sh} is the flow rate of sheath flow, Q_e is the flow rate of excess flow. Fraction of particles with a narrow range of electrically mobility can pass through the DMA. Transfer function (Ω) can be defined as a fraction of particles with the electrical mobility of Z_p that enter the sample flow. The transfer function of DMA is shown in Fig 3.5. $Z_{p,min}$ and $Z_{p,max}$ are the minimum and the maximum electrical mobility of the particles which can enter the sample flow.

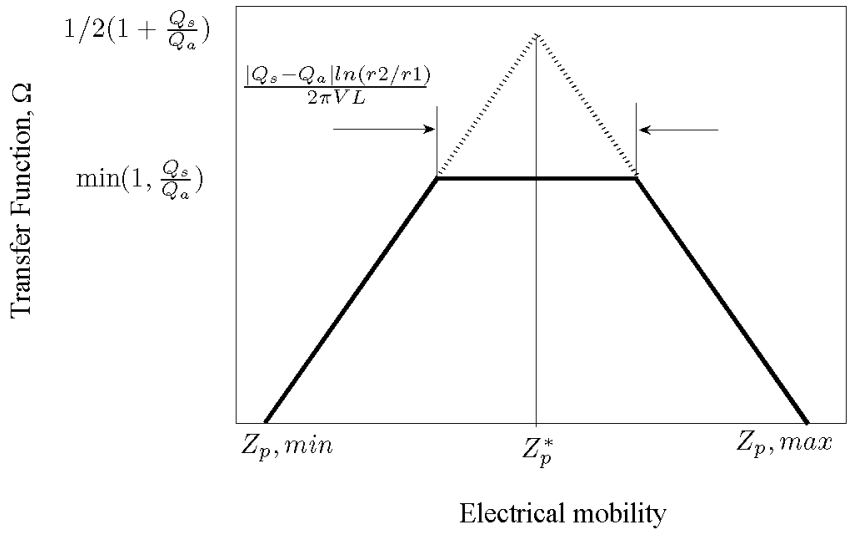

Figure 3.5. The transfer function of DMA

In the DMAs which were used in the experiments (TSI, Model 3776), by default the flow rate of the sample flow is equal to the flow rate of the aerosol flow. As a result the flow rate of the sheath flow and the excess flow are equal. It can be shown that is this state, the ΔZ_{p} which is $(Z_{\mathrm{p,max}} - Z_{\mathrm{p,min}})/2$ can be obtained by

$$\Delta Z_{\mathrm{p}} = \frac{Q_{\mathrm{a}}}{Q_{\mathrm{sh}}} Z_{\mathrm{p}}^{*} \tag{3.12}$$

which shows that the transfer depends on the ratio of the aerosol flow to the sheath flow.

Based on the definition of the mobility diameter the Equation 3.6 can be written as:

$$Z = \frac{neC_c(d_{\mathrm{ve}})}{3\pi\mu\chi d_{\mathrm{ve}}} = \frac{neC_c(d_{\mathrm{m}})}{3\pi\mu d_{\mathrm{m}}} \tag{3.13}$$

which means the relation d_{m} and d_{ve} can be found by:

$$\frac{d_{\mathrm{ve}}}{C_c(d_{\mathrm{ve}})} = \frac{d_{\mathrm{m}}}{\chi C_c(d_{\mathrm{m}})} \tag{3.14}$$

To measure the size distribution of a polydisperse aerosol flow, this highly monodisperse line can be connected to Condensation Particle Counter (CPC). By scanning the voltage and counting the number of concentration via CPC, the size distribution of aerosol particles could be obtain. Figure 3.4 shows the schematic of the DMA.

3.3 CPC

The CPC is kind of an optical particle counter which was introduced by Agarwal and Sem (1978). Two CPCs (TSI, model 3776) were used in this study. This model can detect small particles down to 2.5 nm. The aerosol sample is passed through a capillary and mixed with a sheath flow which contains butanol vapor. Then the mixture of sample flow and sheath flow passes into a cooled condenser. The particles in the sample flow act as condensation nuclei and butanol vapor condenses on them. Due to the condensation of butanol, the particles grow to larger size which can be detected by the optical detector.

3.4 CPMA

The schematic and a photo of centrifugal particle mass analyzer (CPMA) are shown in Fig 3.6. The CPMA consists of two coaxial rotating cylinders. The inner cylinder is connected to a high voltage controller, which attracts negatively charges particles. Thus, these particles experience two different forces: electrostatic force and centrifugal force. Since the direction of these forces are opposite, at a set voltage and speed just particles in a narrow ratio of mass-to-charge will go through the exit slit. These principles of working is similar to the aerosol particle mass analyzer (APM; Ehara et al., 1996), except the inner cylinder in the CPMA rotates slightly faster than the outer one, which increases the amplitude of the transfer function (Olfert et al., 2007).

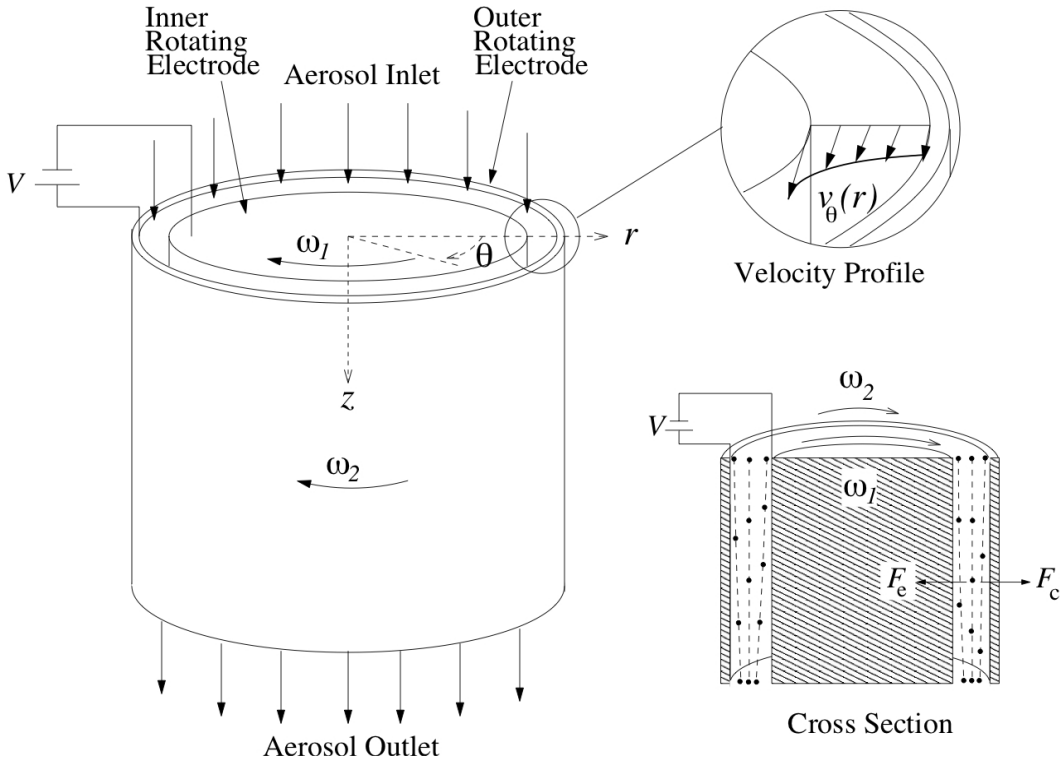

(a)

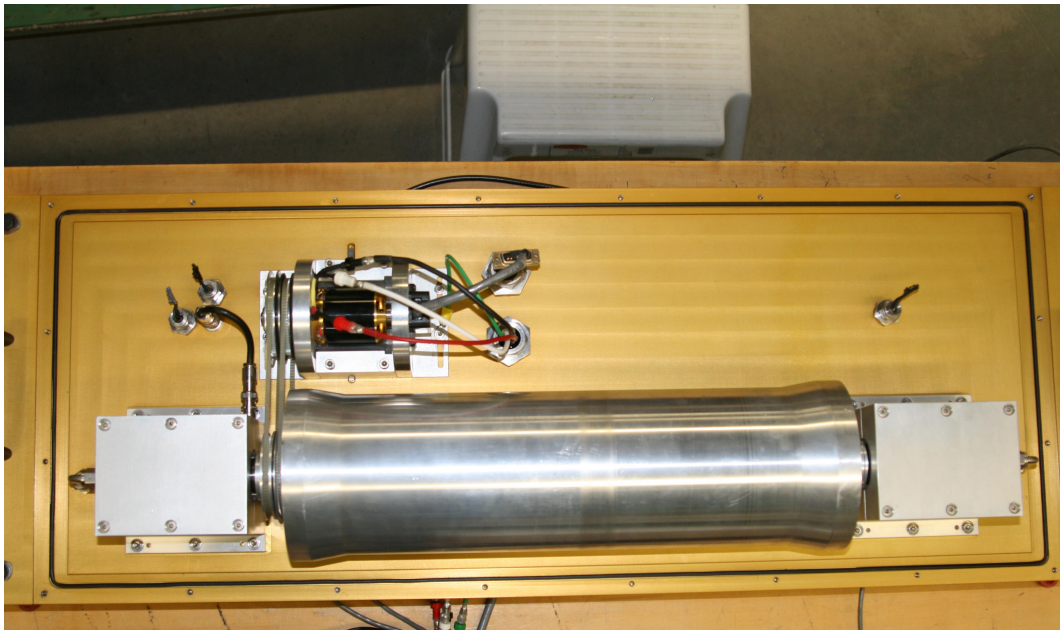

(b)

Figure 3.6. (a) Schematic and (b) photo of CPMA

Similar to the DMA, by connecting the CPMA to a CPC, and scanning the voltage and speed the mass distribution of polydisperse aerosol could be found. However when the inlet aerosol is monodisperse (like aerosol from the DMA), simply scanning the voltage at a set speed is sufficient to find the mass of particles.

A particle in CPMA experiences two forces: electrostatic force (as Eq. 1) and centrifugal force. The trajectory of particles can be find by (Olfert and Collings, 2005):

$$\frac{m}{\tau}\frac{dr}{dt} = \frac{m\left[v_\theta(r)\right]^2}{r} - \frac{neV}{r\ln(\frac{r_2}{r_1})} \tag{3.15}$$

where m is the mass of the particle, τ is the particle relaxation time, t is the time, v_θ is the velocity of the flow in the angular direction, V is the voltage between the two cylinders, n is the number of elementary charges on the particle, e is the unit electrical charge(1.6×10^{-19} C), and r_1 and r_2 are the inner and outer radius of the electrodes. For a monodisperse aerosol the transfer function of the CPMA will be maximum when the centrifugal and electrostatic forces cancel each other at the centre of the gap between the electrodes, then:

$$m_C = \frac{neV_C}{w_C^2 r_C^2 r\ln(\frac{r_2}{r_1})} \tag{3.16}$$

where V_c is the voltage at which the transfer function is maximum, r_c is the average of r_1 and r_2, and ω_c is the angular velocity at r_c.

The transfer function of CPMA is shown in Fig 3.7 as a function of mass-to-charge ratio, s, for $\lambda = 1$. λ is a dimensionless constant and determines the shape of the transfer function and it is defined by (Olfert et al., 2006):

$$\lambda = \frac{L/\bar{v}_z}{1/\{2\tau[(\omega_1(\hat{r}^2 - \hat{\omega})/(\hat{r}^2 - 1))^2 - \omega_1 r_1^2(\hat{\omega} - 1)/(\hat{r}^2 - 1))^2 / r^{*4}]\}} \quad (3.17)$$

where L is the length of the classifier, $\bar{v}_z$ is the average flow velocity in the axial direction, τ is the particle relaxation time, ω_1 and ω_2 are the inner and outer electrode angular velocities, $\hat{\omega} = \omega_2 / \omega_1$ and $\hat{r} = r_2 / r_1$ and r^* is the equilibrium radius.

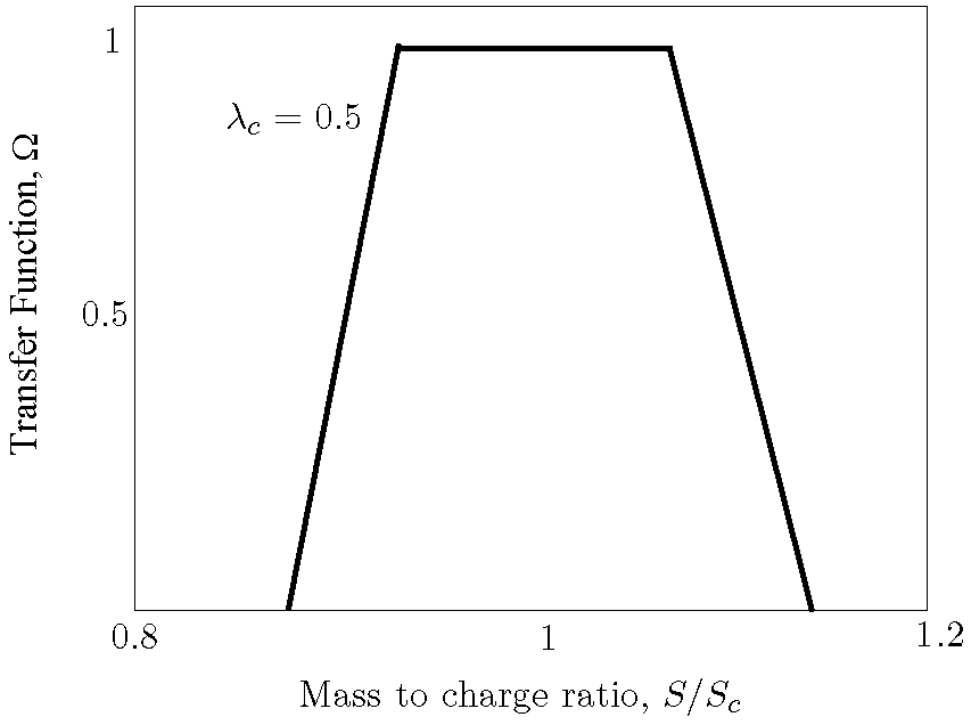

Figure 3.7. The transfer function of CPMA (Olfert and Collings, 2005)

3.5 Coating chamber

A coating chamber was used to coat soot particles with acid or dioctyl sebacate (DOS). The aerosol flow was passed through a coating chamber similar to the design of Moteki and Kondo (2007), which is 20 cm beaker with diameter of 3 cm. Figure 3.8 shows a schematic of the coating chamber. The aerosol flow is coming in from the stopper on top of the beaker. It was partially filled with the coating material and maintained at constant temperature with an oil bath. The bath temperature was held in the range of 95 to 100^{o}C and 112 to 117^{o}C for oleic acid and DOS coating respectively.

3.6 Thermodenuder

To remove the coating on soot particles a thermodenuder has been used in this experiment. The thermodenuder consist of a long piece of copper tubing with two parts: the heating section (6.3 mm in diameter, and 63 cm in length) and the cooling section (6.3 mm in diameter, and 110 cm in length). The heating section was maintained at 200^{o}C and the cooling section maintained at room temperature**.** Activated carbon was not used in the cooling section as it has been shown by Saleh et al. (2011), that is not required to remove volatile material. To check the efficiency of the thermodenuder, experiments were conducted by coating soot particles with thick coatings of dioctyl sebacate (DOS). The mass of size-selected particles before coating with DOS and after a coating and denuding process were compared. The results show no change in mass, which means that the thermodenuder could efficiently take off thick coatings of volatile material from

the soot particles. To minimize the effect of coagulation on the results, the bypass flow paths had the same residence time of the thermodenuder.

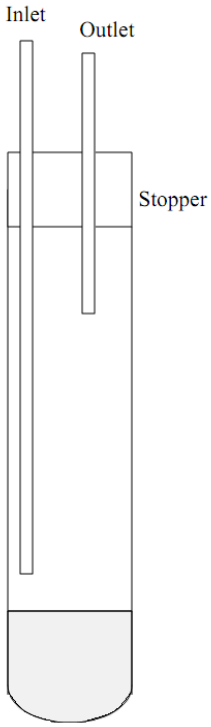

Figure 3.8. Schematic of the coating chamber

3.7 References

Agarwal, J.K., Sem, G.J., 1978. Generating submicron monodisperse aerosol for instrument calibration. *TSI Quarterly* 3-8.

Coderre, A.R., Thomson, K.A., Snelling, D.R., Johnson, M.R., 2011. Spectrally resolved light absorption properties of cooled soot from a methane flame. *Applied Physics B* 104, 175-188.

Ehara, K., Hagwood, C., Coakley, K.J., 1996. Novel method to classify aerosol particles according to their mass-to-charge ratio-aerosol particle mass analyser. *Journal of Aerosol Science* 27, 217-234.

Knutson, E.O., Whitby, K.T., 1975. Aerosol classification by electric mobility: apparatus, theory, and applications. *Journal of Aerosol Science* 6, 443-451.

Maricq, M.M., Harris, S.J., Szente, J.J., 2003. Soot size distributions in rich premixed ethylene flames. *Combustion and Flame* 132, 328 -342.

Moteki, N., Kondo, Y., 2007. Effects of mixing state on black carbon measurements by laser-induced incandescence. *Aerosol Science and Technology* 41, 398-417.

Olfert, J., Reavell, K., Rushton, M., Collings, N., 2006. The experimental transfer function of the Couette centrifugal particle mass analyzer. *Journal of Aerosol Science* 37, 1840-1852.

Olfert, J.S., Collings, N., 2005. New method for particle mass classification - the Couette centrifugal particle mass analyzer. *Journal of Aerosol Science* 36, 1338-1352.

Olfert, J.S., Symonds, J.P.R., Collings, N., 2007. The effective density and fractal dimension of particles emitted from a light-duty diesel vehicle with a diesel oxidation catalyst. *Journal of Aerosol Scienc*e 38, 69 - 82.

Saleh, R., Shihadeh, A., Khlystov, A., 2011. On transport phenomena and equilibration time scales in thermodenuders. A*tmospheric Measurement Techniques* 4, 571-581.

Stipe, C., Higgins, B., Lucasa, D., Koshland, C., Sawyer, R., 2005. Inverted co-flow diffusion flame for producing soot. *Review of Scientific Instruments* 76, 023-908.

Chapter 4: Comparing soot generated from an inverted burn and a McKenna burner and their properties

4.1 Introduction

Soot particles are an important atmospheric constituent that can influence precipitation, visibility and human health. They also can affect climate and Earth's temperature by increasing scattering and absorption of solar radiation. Individual primary spherules in the range of about 15-40 nm aggregate and form the soot particles (Slowik et al., 2007). This aggregation mechanism has an influence on most soot properties including: transport, potential health effects and optical properties. Consequently the study of soot and its properties has received extensive attention.

One of the most common methods to generate black carbon (BC) in climate studies, instrument calibration, and soot morphology studies is by using burners. For example, Zhang et al. (2008) used a Santoro-type laminar diffusion burner to produce soot to study properties of soot aerosols during atmospheric processing. Slowik, et al. (2007) used a pre-mixed McKenna burner to generate soot for instrument comparison.

McKenna burners have been extensively used for generating soot particles from a premixed flame (Migliorini et al., 2008). Maricq et al. (2003) studied the number distribution of soot generated in rich pre-mixed ethylene flames from a McKenna burner with equivalence ratios from Φ=1.79 to Φ=2.44. The equivalence ratio is defined as the ratio of the fuel-to-air ratio to the stoichiometric fuel-to-air ratio.

The soot was sampled from 10 to 25 mm above the burner. Maricq (2004) modified the sampling method and measured the size and the charge of soot particles from the McKenna burner using a nano differential mobility analyzer (DMA).

Maricq and Xu (2004) measured the effective density and mass-mobility exponent of soot particles at Φ=2.04, using a tandem DMA-electrical low pressure impactor (ELPI). Maricq (2007) studied coagulation dynamics of fractal-like soot aggregates. Soot from a McKenna burner (premixed ethylene flame) was rapidly sampled and cooled, and introduced into a residence time flow tube to isolate coagulation from the nucleation and surface growth processes. Cross et al. (2010) also used McKenna burner as soot generator for comparing different instruments. They sampled the soot higher above the burner than Maricq et al. (2003) and Maricq (2007).

Recently, the inverted burner (an inverted co-flow diffusion flame) has been used for generating soot particles. This method of particle generation was introduced by Stipe et al. (2005) and it is capable of generating soot in a wide range of sizes and concentrations. Due to the inverted design the buoyant gases from the downward combustion flow prevent the flame from flickering. Hence, the concentration and size of generated soot is steady with respect to time. Coderre et al. (2011) measured the optical extinction of the soot from the inverted burner. Kirchstetter and Novakov (2007) used the inverted diffusion flame to generate soot particles for thermal–optical analysis by aethalometer. Chakrabarty et al. (2012) studied super-aggregates from an inverted diffusion flame. They measured

mass fractal dimension super-aggregates in the range of 2 to 10 μm by SEM, which yielded mass fractal dimension of 2.5±0.12.

In the present study, the physical properties of the soot generated from McKenna and inverted burner are measured and compared. The physical characteristics of soot from these flames including: the number distributions of mobility-equivalent diameter, mass concentrations, effective density, mass-mobility relation, and fraction of volatile material for each burner have been investigated. This data can be used by researchers to help find operating conditions for these burners, and to determine which burner is the best for a particular application.

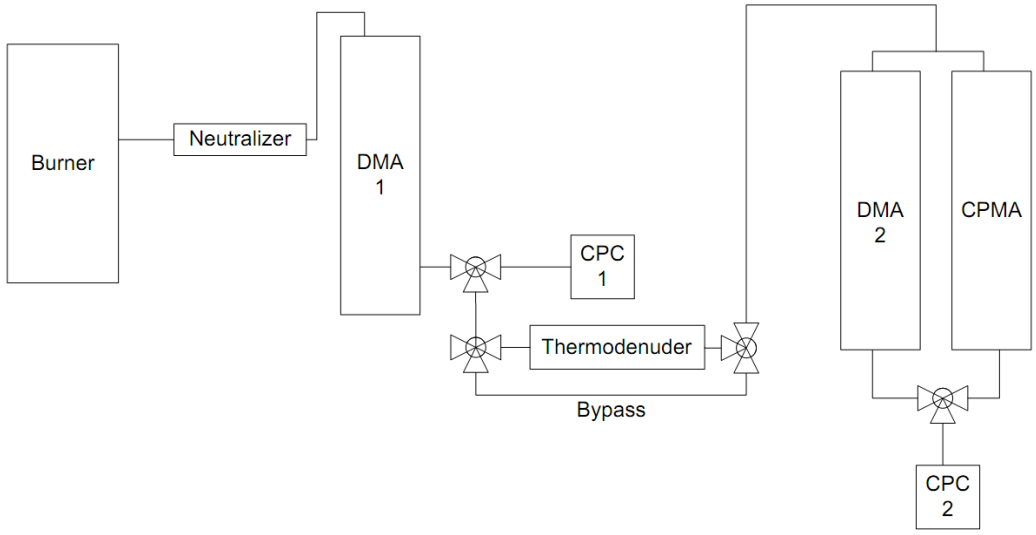

Figure 4.1. Schematic diagram of the experimental setup

4.2 Experimental setup

Figure 4.1 provides the schematic of the experimental setup. The experiment consists of a McKenna burner or an inverted burner, two DMAs (TSI, model 3080), a centrifugal particle mass analyzer (CPMA), two condensation particle

counters (CPC; TSI, Model 3776) and a thermodenuder.

Schematics of both burners are shown in Fig 4.2. Ethylene and air were supplied to the commercially available McKenna burner (Holthuis & Associated, Sebastopol, CA) via mass flow controllers at flow rates of 1.114-2.09 SLPM (Cole-Parmer, model 32907-69) and 8 SLPM (Cole-Parmer, model 32907-71), respectively, to give equivalence ratios over the range of 2 to 3.75. A shroud of nitrogen gas, at flow rates of at 35-45 SLPM, was used to shield the flame from the surrounding atmosphere. This sheath flow of nitrogen is essential to the stability of the flame and provides the first stage of dilution. Lower flow rates of nitrogen can cause the flame to be unstable. The flame was contained by a glass housing minimize the effect of the surrounding atmosphere. The aerosol was sampled 27 cm above the burner and then diluted 15 times with an ejector dilutor.

The inverted burner was based on design of Stipe et al. (2005) and Coderre et al., (2011). The length of quartz tube was 48 cm and its diameter was 48 mm. Methane and air were supplied to the burner via mass flow controllers at flow rates of 1.03-1.26 SLPM (Cole-Parmer, model 32907-69) and 18 SLPM (Omega, model FMA-774-V), respectively, to give equivalence ratios over the range of 0.55 to 0.69. Two stages of dilution were used. Primary dilution air, controlled by another mass flow controller (Omega, FMA-774-V), was injected into the exhaust at a flow rate of 29 to 45 SLPM to maintain the primary dilution ratio at 3.5. Soot particles were sampled 50 cm after the primary dilution by an ejector dilutor with a dilution ratio of 15.

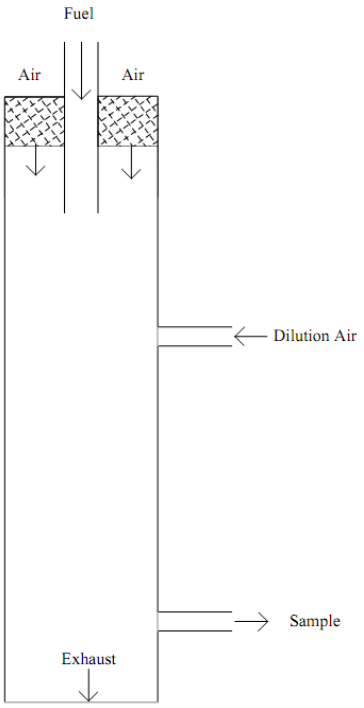

(a)

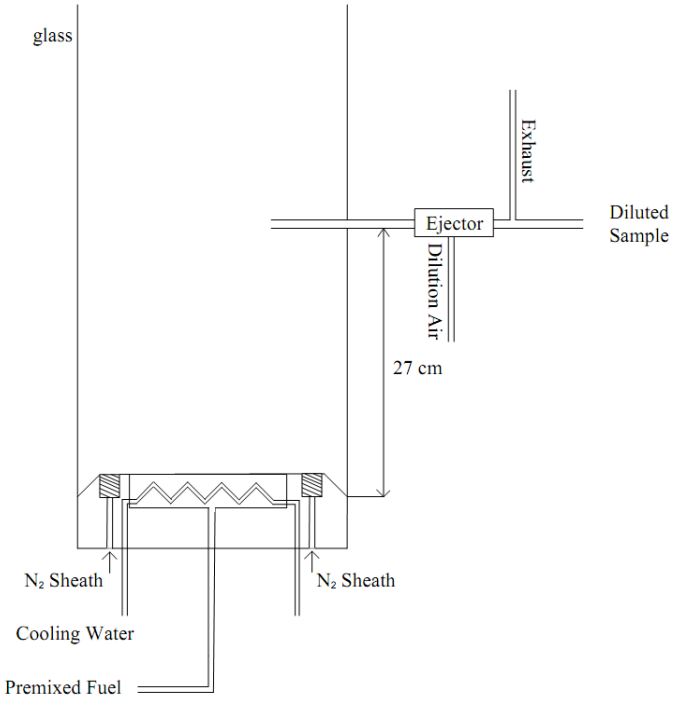

(b)

Figure 4.2. Schematic of (a) the inverted burner and (b) the McKenna burner

Table 4.1. Burners settings and the results

Burner	Equivalence ratio	Primary air or nitrogen dilution flow rate (SLPM)	Total Concentration (#/cm^3)	Median diameter (nm)	Mass-mobility exponent of fresh soot	Total mass concentration (ng/cm^3)
McKenna burner	2	45	3.92×10^7	97.4	2.19	25.49
	2.5	45	4.58×10^7	147.7	2.22	123.54
	3.1	42	6.15×10^7	92.9	2.54	98.39
	3.75	35	6.36×10^7	85.9	2.81	47.15
Inverted burner	0.53	29.3	9.35×10^5	62.25	2.23	0.15
	0.54	30.2	1.64×10^6	79.70	2.21	0.42
	0.55	31	2.36×10^6	102.70	2.21	1.46
	0.57	31.7	4.07×10^6	133.73	2.28	3.72
	0.59	34.4	5.89×10^6	142.70	2.33	7.36
	0.61	36.15	8.25×10^6	153.85	2.41	13.20
	0.63	37.85	1.09×10^7	159.80	2.44	21.23
	0.65	39.55	1.37×10^7	161.85	2.48	29.76
	0.67	41.25	1.70×10^7	163.25	2.54	41.98

The flow settings and the results for both burners are shown in the Table 4.1. The total number concentration and the total mass concentration have been corrected for the second stage of dilution in the ejector.

The DMA classifies particles by their electrical mobility. Two DMAs (TSI, model 3080) were used in this study and are labeled DMA1 and DMA2 in Figure 4.1. DMA 1 contained a Kr-85 neutralizer and the particles were not neutralized in DMA 2. Number distribution measurements were made by using DMA1 and CPC1 in an SMPS system. The aerosol flow rate in the DMA was set to 0.3 LPM and the sheath flow was set to 3 LPM. The number distribution was calculated using the inversion scheme implemented in TSI's Aerosol Instrument Manager (AIM, version 9.0).

Mass and effective density measurements were made using DMA1, the CPMA, and CPC2. The CPMA consists of two concentric rotating electrodes. Charged particles passing between the electrodes experience centrifugal and electrostatic forces and particles of a narrow range of mass-to-charge ratio exit the instrument (Olfert and Collings, 2005). The CPMA was a custom design with an inner radius of 60 mm, and outer radius of 61.5 mm, and length of 400 mm. The full-width half-maximum resolution of the CPMA was generally set to 0.2. For measuring the mass of particles a sample flow of 1.5 LPM was maintained through DMA1, the CPMA, and CPC2. The sheath flow of DMA1 was held between 8 to 15 LPM depending on the particle size. To obtain the mass of volatile material on the particles, the sample flow passed through a thermodenuder after DMA1 and the mass of particles was compared to the uncoated mass.

The thermodenuder consist a long piece of copper tubing with two parts: the heating section (6.3 mm in diameter, and 63 cm in length) and the cooling section (6.3 mm in diameter, and 110 cm in length). The heating section was maintained at 200^{o}C and the cooling section was maintained at room temperature**.** Activated carbon was not used in the cooling section as it has been shown by Saleh et al. (2011), that is not required to remove volatile material. To check the efficiency of the thermodenuder, experiments were conducted by coating soot particles with thick coatings of dioctyl sebacate (DOS). The mass of size-selected particles before coating with DOS and after a coating and denuding process were compared. The results show no change in mass, which means that the

thermodenuder could efficiently take off thick coatings of volatile material from the soot particles.

The thickness of the volatile material on the particles was measured using DMA1, DMA2, and CPC2. The sample flow through the instruments was 1.5 LPM and the sheath flow was held between 8 to 15 LPM (depending on the particle size) for both DMAs. After passing through the neutralizer in DMA1, the sample flow passed through the thermodenuder (or by-pass) and its mobility diameter was measured using DMA2 and CPC2. DMA2 was setup using an automated voltage-stepping routine, where the measured mobility diameter was the mobility diameter corresponding to the maximum concentration on CPC2.

4.3 Results and discussion

4.3.1 Particle number distribution

Figure 4.3 shows number distributions for both the inverted burner and the McKenna burner at different equivalence ratios. In the inverted burner, both the mode mobility-equivalent particle diameter and total number of concentration increases with increasing equivalence ratio. In the McKenna burner, the total number of concentration increases, but the mode diameter decreases more than 40 percent by increasing the equivalence ratio from 2.5 to 4.1. This could be explained by noticing that in the McKenna burner at Φ=2.5 the number distribution evolves into a bimodal distribution. As will be shown Section 4.3.2, this also corresponds to a large increase in the volatile fraction of the particles.

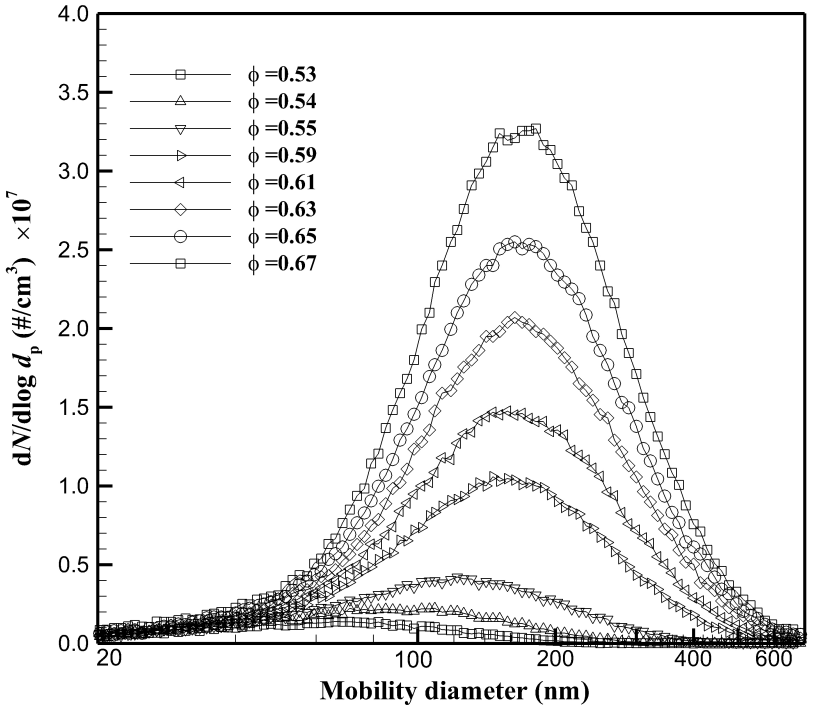

(a)

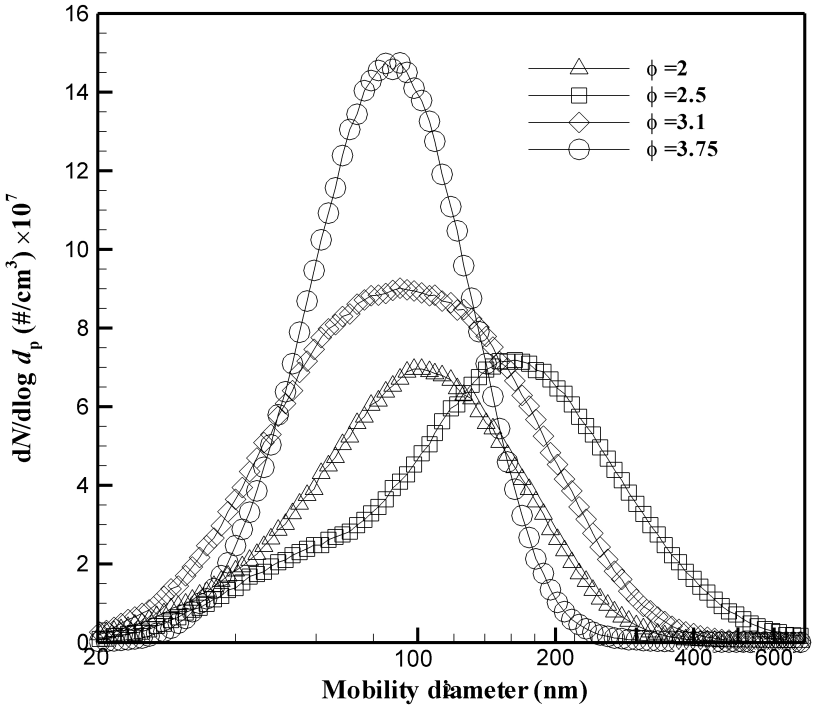

(b)

Figure 4.3. Soot particle number distributions from (a) inverted co-flow diffusion flame (inverted burner) and (b) premixed ethylene flames (McKenna burner) at different equivalence ratios

Maricq (2004) showed that the lower mode arises from new particle nucleation that continues well beyond the flame front.

The mean diameter and the total number concentration as a function of equivalence ratio for the inverted burner are shown in Fig 4.4. The results from Stipe et al. (2005) are also provided for comparison. Although the range of the equivalence ratio is slightly different in their study, the mean particle diameter measured in this study follows a similar trend. In both studies the mean particle diameter increases sharply with increasing equivalence ratio before reaching a constant value. The total number concentration increases linearly with equivalence ratio which is in agreement with Stipe et al. (2005). However, comparing the value of the number concentration is not possible because Stipe et al. (2005) did not give the exact value of dilution ratio for the reported total number of concentration.

4.3.2 Fraction of volatile material

Kirchstetter and Novakov (2007) used laser fragmentation-fluorescence spectroscopy to show that the soot particles generated by the inverted burner have no measurable organic material on them. Our direct measurement of the mass of soot particles with the CPMA before and after passing through a thermodenuder at 200^{o}C confirms that there is not a measureable amount of volatile material on

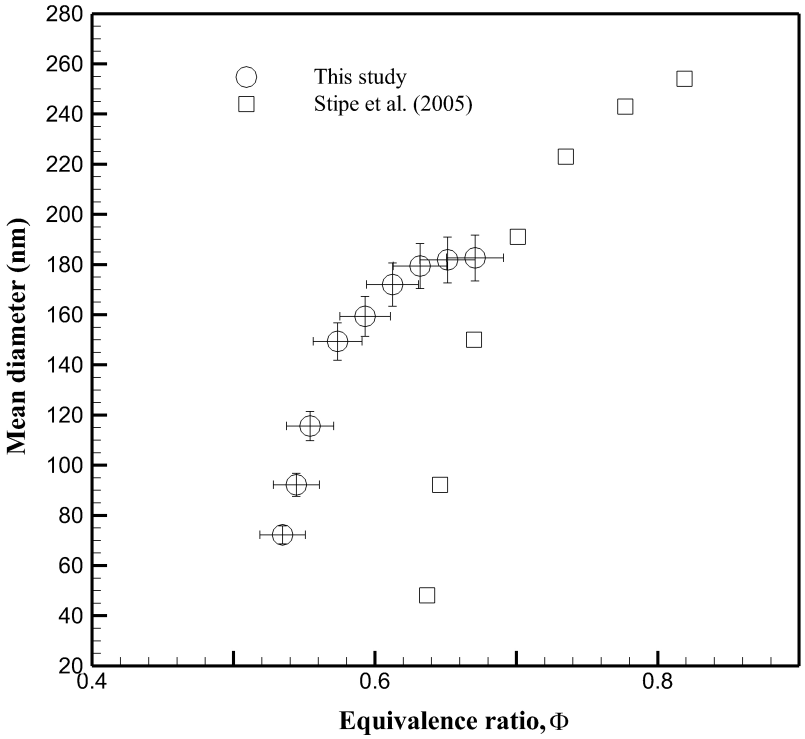

(a)

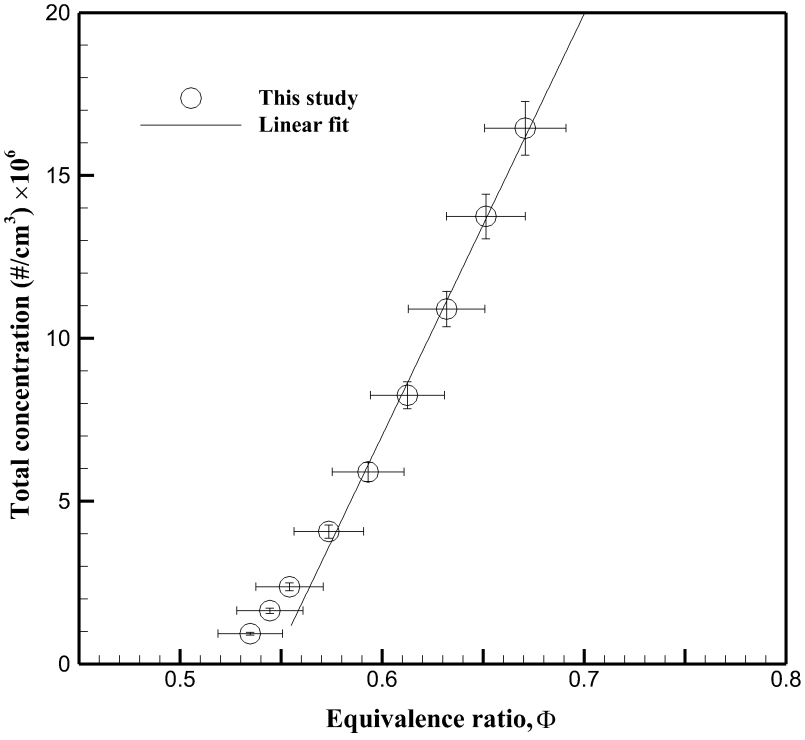

(b)

Figure 4.4. (a) Mean diameter and (b) total number of concentration (not corrected for dilution) at different equivalence ratios for inverted burner

the generated soot from the inverted burner. However, the soot particles generated from the McKenna burner can have a substantial amount of coating. The change in mobility diameter and mass after denuding the coating layer are shown in Fig 4.5. It can be seen from this figure that the mass fraction of coating depends strongly on the equivalence ratio and mobility diameter of the nascent soot. The mass and thickness of coating increase with increasing equivalence ratio. The maximum amount of coating is associated with the equivalence ratio of 3.75. At this equivalence ratio the mass of coating was as high as 5 times the mass of the non-volatile fraction but is relatively independent of particle size. For all other equivalence ratios, as the diameter of particles increases, the fraction of mass coating decreases. However, as it can be seen in Fig 4.6, the absolute mass of volatile material increases with increasing the mobility diameter.

Slowik et al. (2007) and Cross et al. (2010) reported the mass fraction of non-volatile material of the internally mixed particles generated in a McKenna burner. They extracted the soot particles further away from the flame compared to Maricq (2007). They reported that the mass fraction of the internally mixed particles decreased as the equivalence ratio increased which is consistent with the results of the present study. In particular, Cross et al. (2010) showed that the volatile mass fraction of internally mixed particles produced at $\Phi=2.0 \pm 0.2$ is on average 0.26 (which is similar to the value found here) while particles produced at $\Phi=5.0 \pm 0.2$ have a volatile mass fraction of 0.68.

Maricq (2007) also studied the volatility of coating on soot particles generated from the McKenna burner. Maricq examined equivalence ratios between 2.0 and

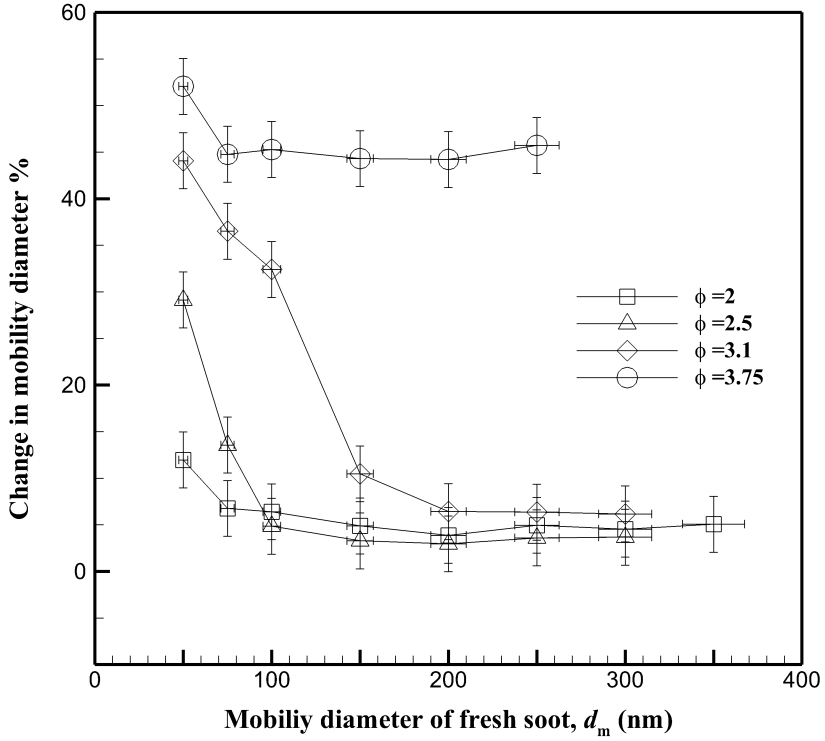

(a)

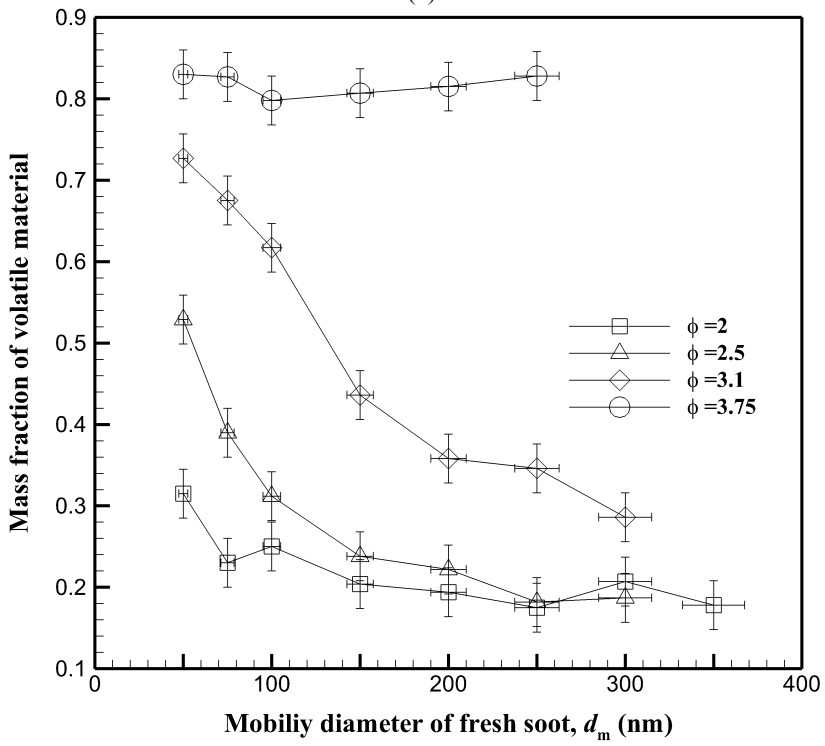

(b)

Figure 4.5. Change in (a) mobility diameter and (b) mass fraction of volatile material on soot generated from McKenna burner

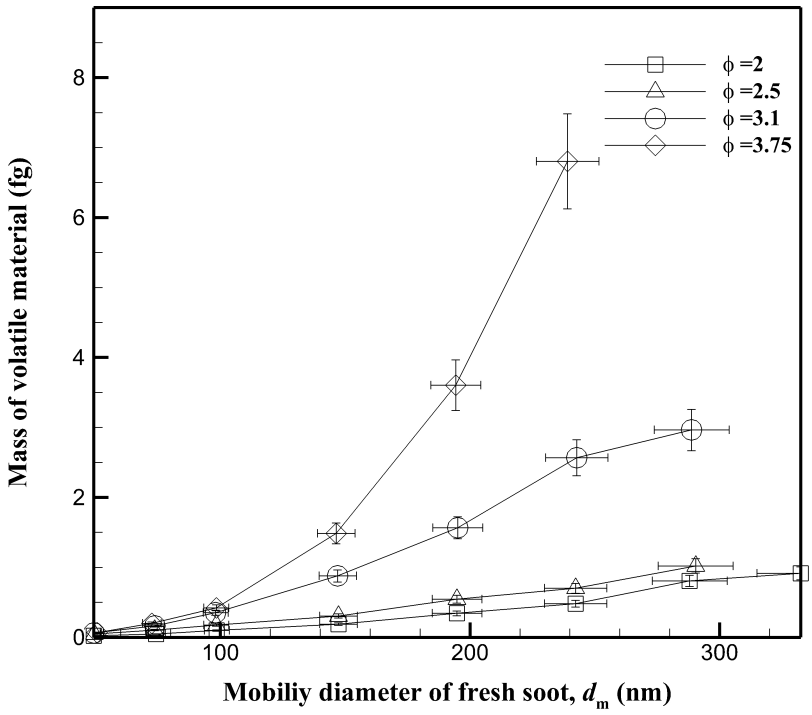

Figure 4.6. Absolute mass of volatile material on soot particles from the McKenna burner at different equivalence ratios

2.4, and diluted the samples much nearer the burner (between 10 to 20 mm above the burner) than this study (27 cm above the burner). Maricq (2007) showed that heating the particles (generated at Φ= 2.4 and extracted at 20 mm above the burner), to 330°C had no effect on their mobility diameter, suggesting there was relatively little volatile material on the particles. In contrast, particles sampled 10 mm above the burner and at Φ= 2.0 show considerable decreases in diameter at denuder temperatures of 330°C, which ranged from 22–32%. Maricq concluded that soot sampled from higher in the flame, or at higher equivalence ratio, show negligible change in size; so, presumably, there was only small amounts of semi volatile content. This trend differs from results of this study as well as Slowik et al. (2007) and Cross et al. (2010). However, this is due to the rapid dilution that

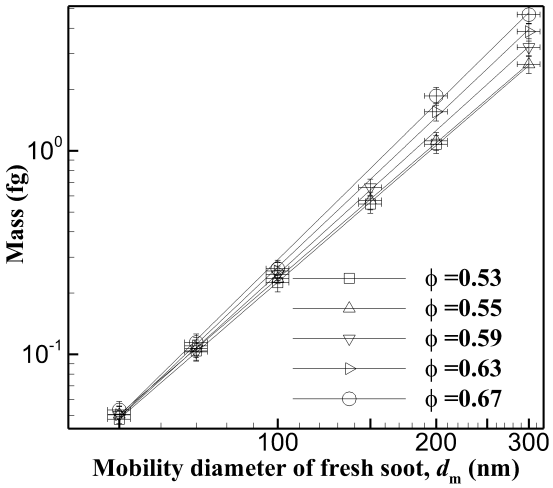

(a)

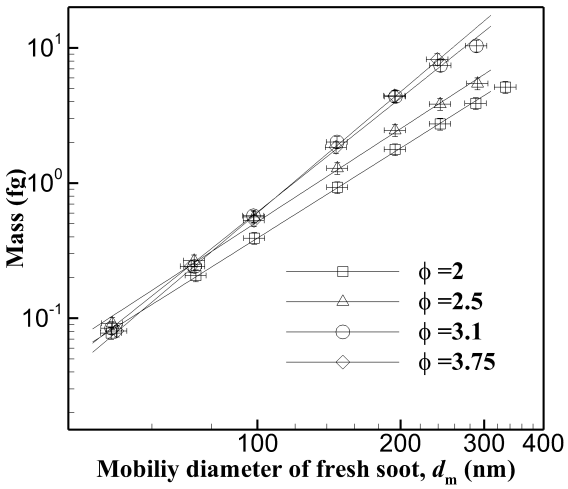

(b)

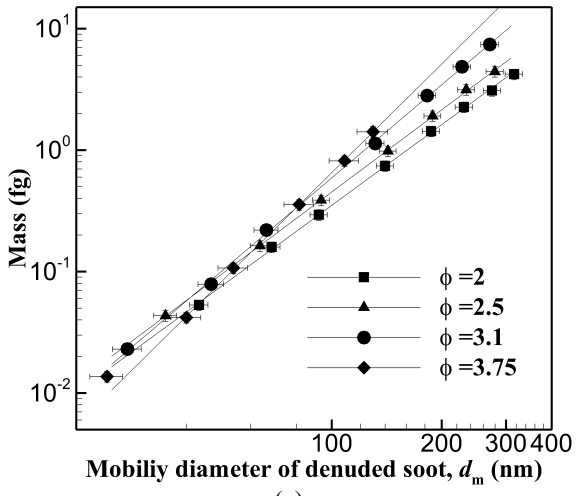

(c)

Figure 4.7. The size-dependent mass of particles from (a) the inverted burner and the (b) McKenna burner without denuding (internally mixed particles) (c) and after denuding (only the non-volatile fraction).

Maricq uses which suppresses the completion of chemical reactions, nucleation, and surface growth processes.

4.3.3 Mass-mobility relationship

The particle mass-mobility relationship for the inverted burner and McKenna burner is shown in Fig. 4.7. It has been shown that the relation between mass (m) and mobility diameter (d_m) can be described by (Park et al., 2003),

$$m = Cd_m^{D_{fm}} \tag{5.1}$$

where C is a constant and D_{fm} is the mass-mobility exponent. The mass-mobility exponent is not the fractal dimension although it is often presented in the literature as such (Kim et al., 2009). However, for both parameters a higher value represents a more spherical particle where a perfectly spherical particle would have a mass-mobility exponent or fractal dimension of 3. In the mass-mobility plots shown in Fig 4.7, the steeper slope represents a higher mass-mobility exponent and, therefore, a more spherical particle.

The variation of mass-mobility exponent as a function of equivalence ratio for both burners is shown in Fig 4.8. In the inverted burner, particles do not contain a volatile component so there is no difference between fresh and denuded results. However, for the McKenna burner the mass-mobility exponent decreases by denuding. The mass-mobility exponent of fresh soot is larger because the liquid volatile material fills the voids in the particle making them more spherical. In both burners the mass-mobility exponent increases with increasing equivalence ratio.

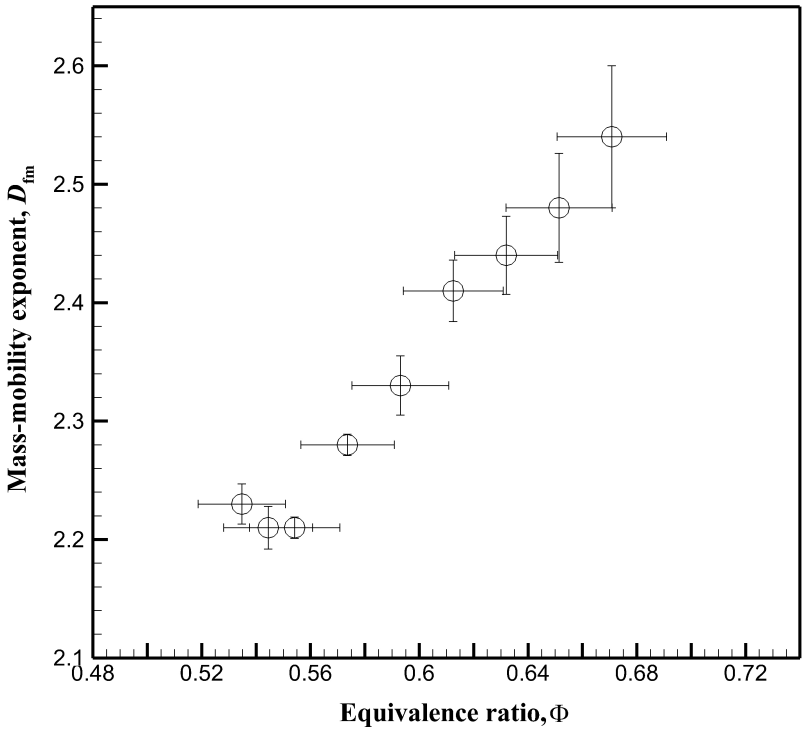

(a)

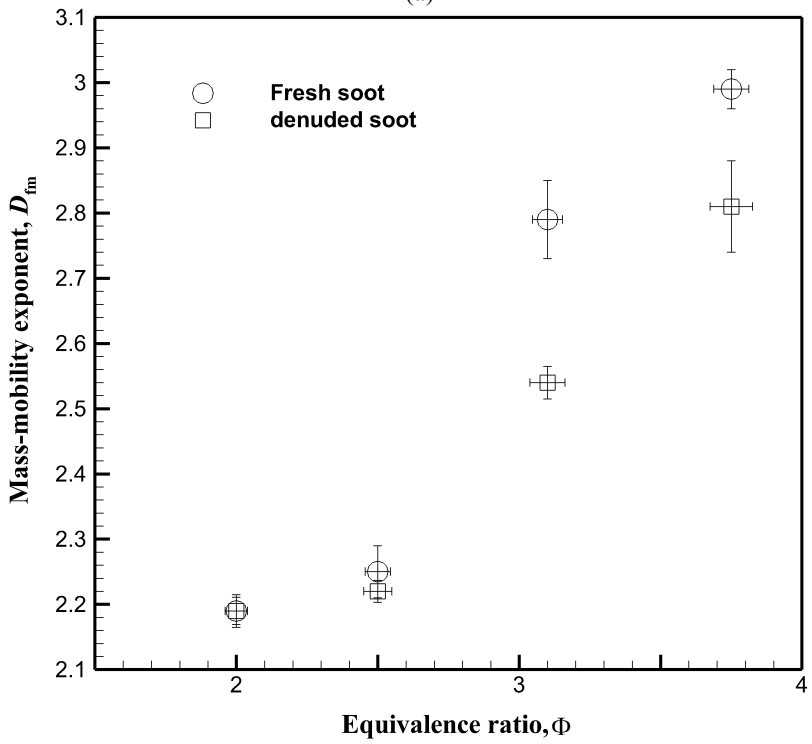

(b)

Figure 4.8. Mass-mobility exponent at different equivalence ratios for (a) the inverted burner and (b) the McKenna burner

In the inverted burner the mass-mobility exponent ranged from 2.23 to 2.54 and in the McKenna burner it ranged from 2.19 to 2.99. Cross et al. (2010) reported the mass-mobility exponent of fresh soot from the McKenna burner to be D_{fm} =2.24 and 3.04 for equivalence ratios of Φ=2.0 and Φ=5, respectively, which agree well with the results in this study. At Φ=2.0, Cross et al. (2010) found the mass-mobility exponent decreased from D_{fm} =2.24 to D_{fm} =2.12 by denuding. In this study, a small amount of volatile material was measured on the particle at an equivalence ratio of 2.0 (see Fig 4.5), however, removing the material with the denuder did not produce a measurable change in the mass-mobility exponent.

The effective density of a particle has an important role in particle transport properties. It is also required for calculating mass distributions from number distributions and finding the relationship between mobility diameter and aerodynamic diameter (Park et al., 2003). When particles are spherical without any internal voids, the density of particles can be calculated by knowing the mass and diameter of the particle. When particles are not spherical, like soot particles, another diameter such as mobility equivalent diameter (d_{me}) can be used. This equivalent diameter may be used to calculate "effective" or "apparent" density (DeCarlo et al., 2004), which will be lower than the material particle density. McMurry et al. (2002) used DMA and APM to measure effective density, the same technique has been employed for a DMA-CPMA system (Olfert et al., 2007). The effective density defined as,

$$\rho_{\text{eff}} = \frac{m}{\frac{\pi}{6} d_{\text{m}}^3} \tag{5.2}$$

Figures 4.9 and 4.10 show the effective density of soot particles versus mobility diameter for different equivalence ratios in the inverted and the McKenna burner, respectively. In general, the effective density decreases as mobility diameter increases. It also can be seen from the figures that increasing the equivalence ratio causes the effective density to increase. For the soot generated from the McKenna burner it can be seen that for small particles denuding increases the effective density, but for larger particles the effective density decreases upon the denuding. This is explained by realizing that the material density of soot is approximately two times of the material density of many organic coatings. Thus for small particles, comprised of a small number of primary particles, the denuding would cause the effective density of particles to increase, and approach the material density of the soot. However, at larger mobility diameters the effective density of the soot core is far below the material density due to the agglomerated nature of the particles. As a result, the volatile material, which fills the internal and external voids, would increase the effective density.

The general trend of decreasing effective density with increasing mobility diameter was not evident for the McKenna burner at Φ=3.75 for denuded particles. At this equivalence ratio, the effective density is constant at mobility diameters greater than 75 nm. This could be caused by compact agglomerates with internal voids. The sharp jump at a mobility diameter at 50 nm could indicate a transition where the mobility size approaches the primary particle size and there are no longer any internal voids.

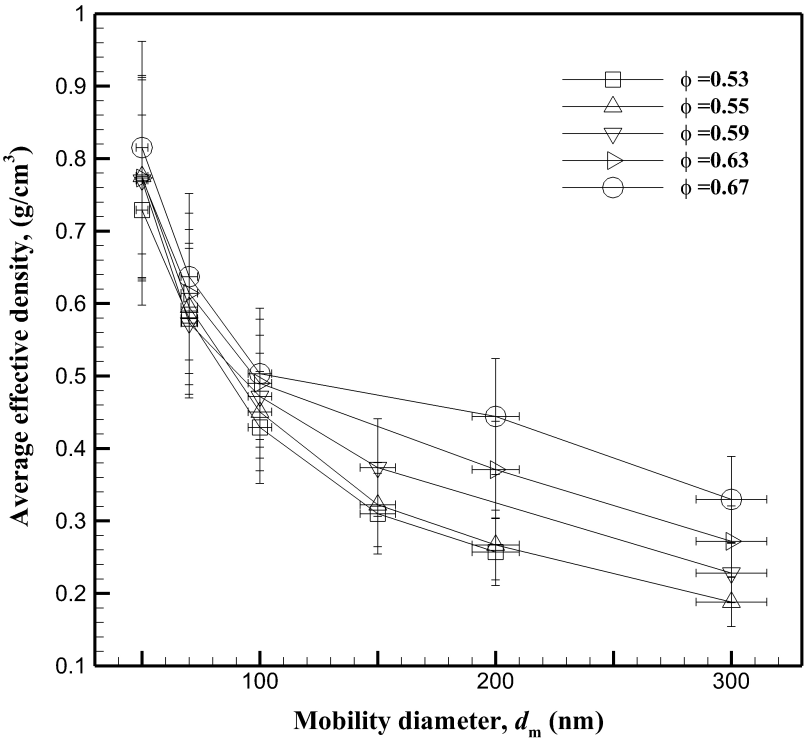

Figure 4.9. Density of soot particles generated from the inverted burner at different equivalence ratios

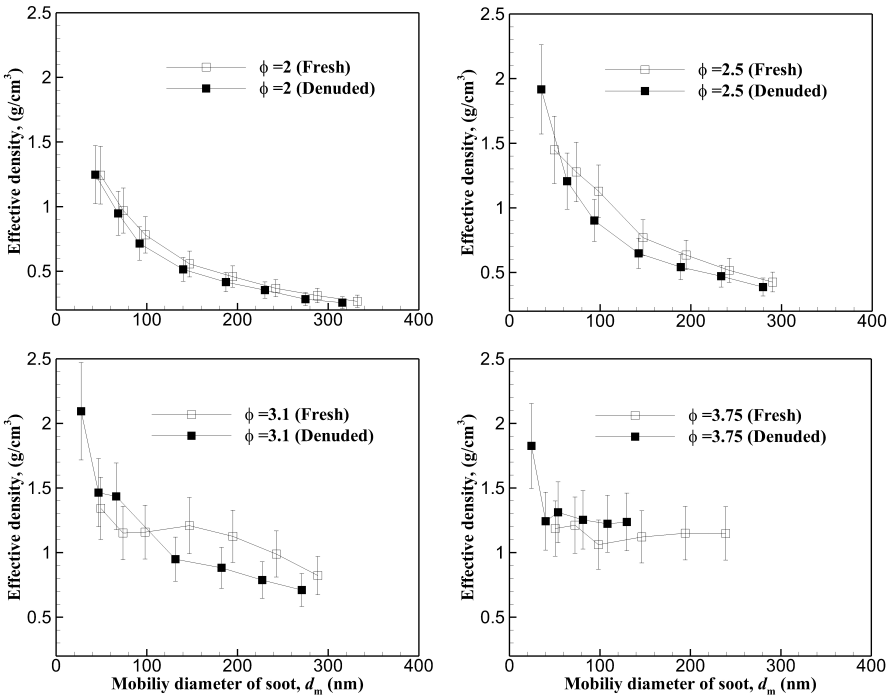

Figure 4.10. Density of fresh and denuded soot particles generated from the McKenna burner

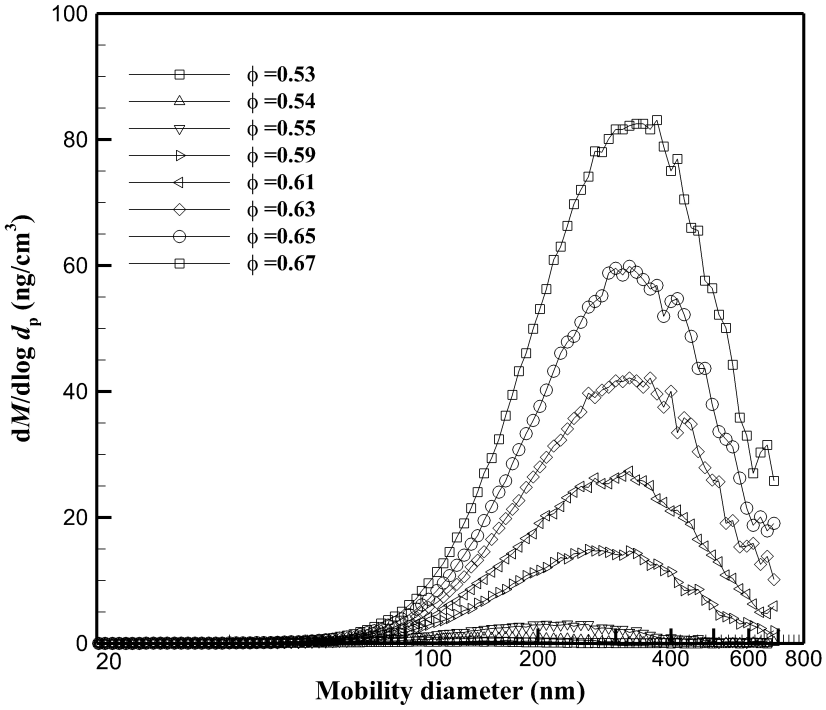

(a)

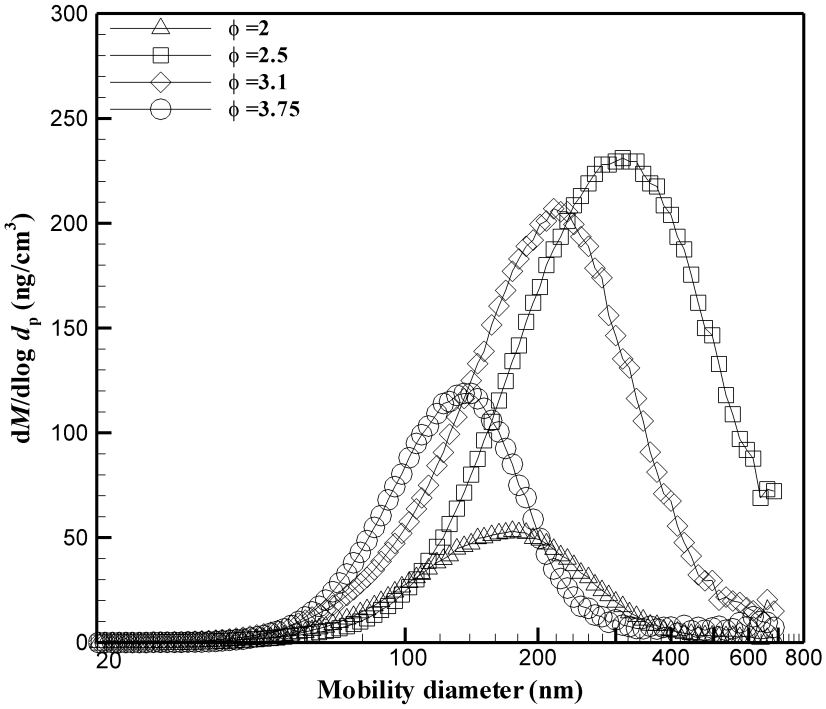

(b)

Figure 4.11. The mass distribution from (a) inverted burner and (b) McKenna burner at different equivalence ratios

4.3.4 Mass distributions and total mass concentration

The effective density can be used to find mass distribution of soot particles from the number distribution. The mass distribution for both inverted and McKenna burners are shown in Fig 4.11 and the total mass concentration is reported in Table 4.1. In the inverted burner, as expected, increasing the equivalence ratio increases total mass concentration. In McKenna burner, increasing the equivalence ratio increases the total number concentration but decreases the total mass concentration, since the size of particles becomes smaller. As one can see from Table 4.1, the total mass concentration decreases more than 20% with an increase in the equivalence ratio from 2.5 to 3.75.

4.4 Conclusion

The number distribution, volatile mass fraction, effective density, mass concentration and mass-mobility exponent of particles from an inverted burner and a McKenna burner were measured with a DMA and a CPMA. It was found that the inverted burner is not just capable of generating soot in a wide range of sizes (mean diameter changed from 72.2 to 182.9 nm) and concentrations (from 9.35×10^5 to 1.7×10^7 #/cm^3) but it can produce soot at different mass-mobility exponent ranges from 2.23 to 2.54 over a range of equivalence ratio of 0.55 to 0.69. With increasing equivalence ratio the mean diameter always increased in the inverted burner, but in the McKenna burner the mean diameter does not follow a simple trend.

The mass-mobility exponent of the soot generated from McKenna burner ranges from 2.19 to 2.99 for fresh soot and 2.19 to 2.81 for denuded soot. In both burners increasing the equivalence ratio caused an increase in the mass-mobility exponent. The effective density of soot generated from both burners, increases with increasing the equivalence ratio.

The soot generated from the inverted burner does not have any measurable volatile material, but the soot generated from the McKenna burner could be have a mass of volatile material up to 5 times the mass of the non-volatile core particle. Although in both burners increasing the equivalence ratio caused an increase in total concentration, in the McKenna burner the total generated mass can decrease by further increasing the equivalence ratio.

One purpose of this work was to provide data so that an appropriate burner and flow settings could be chosen for particular applications. The inverted burner can provide a stable source of black carbon particles with little volatile material, although the range in particle morphology is relatively small. Alternatively, the McKenna burner can produce a wide range in particle morphology but at higher equivalence ratios there can be a considerable amount of volatile material condensed on the particle. The total concentration number and total mass that the McKenna burner can provide is much higher than the inverted burner. However, in the McKenna burner, the shroud of nitrogen gas, especially at higher equivalence ratios, must be in a narrow range to make the flame stable thus limiting the range of primary dilution. However, in the inverted burner, the primary dilution air can be selected without restriction.

4.5 References

Chakrabarty, R.K., Moosmüller, H., Garro, M. A., Stipe, C.B., 2012. Observation of superaggregates from a reversed gravity low-sooting flame. *Aerosol Science and Technology* 46, i-iii.

Coderre, A.R., Thomson, K.A., Snelling, D.R., Johnson, M.R., 2011. Spectrally resolved light absorption properties of cooled soot from a methane flame. *Applied Physics B* 104, 175-188.

Cross, E., Onasch, T., Ahern, A., Wrobel, W., Slowik, J.G., Olfert, J., Lack, D., Massoli, P., Cappa, C., Schwarz, J., Spackman, J.R., Fahey, D., Sedlacek, A., Trimborn, A., Jayne, J., Freedman, A., Williams, L., Ng, N., Mazzoleni, C., Dubey, M., Brem, B., Kok, G., Subramanian, R., Freitag, S., Clarke, A., Thornhill, D., Marr, L., Kolb, C., Worsnop, D., Davidovits, P., 2010. Soot particle studies—instrument inter-comparison—project overview. *Aerosol Science and Technology* 44, 592-611.

DeCarlo, P., Slowik, J.G., Worsnop, D., Davidovits, P., Jimenez, J., 2004. Particle morphology and density characterization by combined mobility and aerodynamic diameter measurements. part 1: Theory. *Aerosol Science and Technology* 38, 1185-1205.

Kim, S.C., Wang, J., Emery, M.S., Shin, W.G., Mulholland, G.W., Pui, D.Y.H., 2009. Structural property effect of nanoparticle agglomerates on particle penetration through fibrous filter. *Aerosol Science and Technology* 43, 344-355.

Kirchstetter, T.W., Novakov, T., 2007. Controlled generation of black carbon particles from a diffusion flame and applications in evaluating black carbon measurement methods. *Atmospheric Environment* 41, 1874-1888.

Maricq, M., 2007. Coagulation dynamics of fractal-like soot aggregates. *Journal of Aerosol Science* 38, 141-156.

Maricq, M., Xu, N., 2004. The effective density and fractal dimension of soot particles from premixed flames and motor vehicle exhaust. *Journal of Aerosol Science* 35, 1251-1274.

Maricq, M.M., 2004. Size and charge of soot particles in rich premixed ethylene flames. *Combustion and Flame* 137, 340-350.

Maricq, M.M., Harris, S.J., Szente, J.J., 2003. Soot size distributions in rich premixed ethylene flames. *Combustion and Flame* 132, 328 -342.

McMurry, P.H., Wang, X., Park, K., Ehara, K., 2002. Relationship between mass and mobility for atmospheric particles. *Aerosol Science and Technology* 36, 227-238.

Migliorini, F., Deiuliis, S., Cignoli, F., Zizak, G., 2008. How "flat" is the rich premixed flame produced by your McKenna burner? *Combustion and Flame* 153, 384-393.

Olfert, J.S., Collings, N., 2005. New method for particle mass classification - the Couette centrifugal particle mass analyzer. *Journal of Aerosol Science* 36, 1338-1352.

Olfert, J.S., Symonds, J.P.R., Collings, N., 2007. The effective density and fractal dimension of particles emitted from a light-duty diesel vehicle with a diesel oxidation catalyst. *Journal of Aerosol Science* 38, 69-82.

Park, K., Cao, F., Kittelson, D.B., McMurry, P.H., 2003. Relationship between particle mass and mobility for diesel exhaust particles. *Environmental Science & Technology* 37, 577-583.

Saleh, R., Shihadeh, A., Khlystov, A., 2011. On transport phenomena and equilibration time scales in thermodenuders. *Atmospheric Measurement Techniques* 4, 571-581.

Slowik, J.G., Cross, E.S., Han, J.-H., Davidovits, P., Onasch, T.B., Jayne, J.T., Williams, L.R., Canagaratna, M.R., Worsnop, D.R., Chakrabarty, R.K., Moosmüller, H., Arnott, W.P., Schwarz, J.P., Gao, R.-S., Fahey, D.W., Kok, G.L., Petzold, A., 2007. An inter-comparison of instruments measuring black carbon content of soot particles. *Aerosol Science and Technology* 41, 295-314.

Slowik, J.G., Cross, E.S., Han, J.-H., Kolucki, J., Davidovits, P., Williams, L.R., Onasch, T.B., Jayne, J.T., Kolb, C.E., Worsnop, D.R., 2007. Measurements of morphology changes of fractal soot particles using coating and denuding experiments: implications for optical absorption and atmospheric lifetime. *Aerosol Science and Technology* 41, 734-750.

Stipe, C., Higgins, B., Lucasa, D., Koshland, C., Sawyer, R., 2005. Inverted co-flow diffusion flame for producing soot. *Review of Scientific Instruments* 76, 023908.

Zhang, R., Khalizov, A.F., Pagels, J., Zhang, D., Xue, H., McMurry, P.H., 2008. Variability in morphology, hygroscopicity, and optical properties of soot aerosols during atmospheric processing. *Environmental Sciences* 105, 10291-6.

Chapter 5: Soot aggregate restructuring due to coatings of oleic acid and dioctyl sebacate

5.1 Introduction

It is generally accepted that aerosols are an important atmospheric constituent that can influence precipitation, visibility, and human health. They also can affect climate and Earth's temperature by the scattering and absorption of solar radiation. Black carbon (BC) from the burning of fossil fuel and biomass has a large positive component of radiative forcing compared to other aerosols (Jacobson, 2001). Freshly emitted soot particles are hydrophobic and fractal aggregates (Slowik et al., 2007) and mostly externally mixed with non-refractory compounds (Shiraiwa et al., 2007). Once emitted into the atmosphere, BC particles undergo an aging process, and they will become internally mixed. The internally mixed BC particles can be referred to as "coated" (McMeeking et al., 2011) and this coating of non-refractory compounds (such as sulfate and organic materials) can change the optical properties of BC (absorbing, scattering, etc.) as well as its morphology. Several studies have investigated the effect of coatings on particle morphology. These studies have shown that coatings can cause soot particles to restructure to a more compact shape. This will change the optical properties of the particles, which ultimately changes how these particles affect Earth's climate.

Slowik et al. (2007) studied the effect of coating on the morphology of soot generated from a premixed ethylene/oxygen flame. They coated particles with oleic acid and anthracene and measured their properties such as mass, volume, density, composition, dynamic shape factor, mass-mobility exponent, surface area by an Aerodyne aerosol mass spectrometer and a scanning mobility particle sizer (SMPS). Slowik et al. (2007) qualitatively showed that oleic acid coating caused the BC particles collapse into more compact shape.

Zhang et al. (2008) investigated variability in morphology, hygroscopicity, and optical properties of soot aerosols during atmospheric processing. They reported soot particles exposed to sulfuric acid vapor exhibit a noticeable change in morphology, characterized by a decrease in the mobility-based diameter and an increase in the mass-mobility exponent and effective density. They found that coating with sulfuric acid increased the scattering and the absorption of the particles.

Xue et al. (2009a) studied effects of dicarboxylic acid coating on absorption and scattering of visible light by soot. They observed that internal mixing of soot aerosol with dicarboxylic acids substantially enhanced light scattering and to some degree increased light absorption. Xue et al. (2009b) studied effects of coating with dicarboxylic acids on mass-mobility relationship of soot particles. They observed that coatings of succinic acid did not restructure the soot core while glutaric acid coatings did cause restructuring. Xue et al. (2009b) suggest the difference in the restructuring could be due to the difference in melting point of the acids.

Pagels et al. (2009) also investigated soot particle morphology using controlled condensation of sulfuric acid and water vapor into laboratory generated flame soot. They reported for a specified soot source and condensing liquid, the degree of restructuring depends highly on the mass fraction of condensed material.

Cross et al. (2010) also studied changes in the morphology and optical properties of soot particles with coatings of sulfuric acid and dioctyl sebacate. They reported the sulfuric acid coating caused the fractal soot core to restructure to a more compact configuration but the dioctyl sebacate (DOS) coating did not affect the morphology of the original soot core.

Soot particles in the atmosphere can have different amounts of coating (Shiraiwa et al., 2007), and the properties of soot can change depend on coating thickness. Although some of the above studies suggest that the coating thickness is an important factor for degree of collapsing, none have systematically investigated the effect of coating thickness with a wide range of coating thicknesses or as a function of the initial particle size. In this study, the effect of coating thickness on the morphology of soot particles is investigated using oleic acid and DOS coatings. The reason for choosing these two coating materials is they easily condense on the soot particles, and do not readily nucleate. A wide range of coating thicknesses was used, with up to 12 times as much coating as the mass of the soot.

5.2 Experimental setup

Figure 5.1 provides the schematic of the experiment. The experiment consist of a

burner, differential mobility analyzer (DMA; TSI model 3080), a centrifugal particle mass analyzer (CPMA), two condensation particle counters (CPC; TSI, Model 3776) and a thermodenuder.

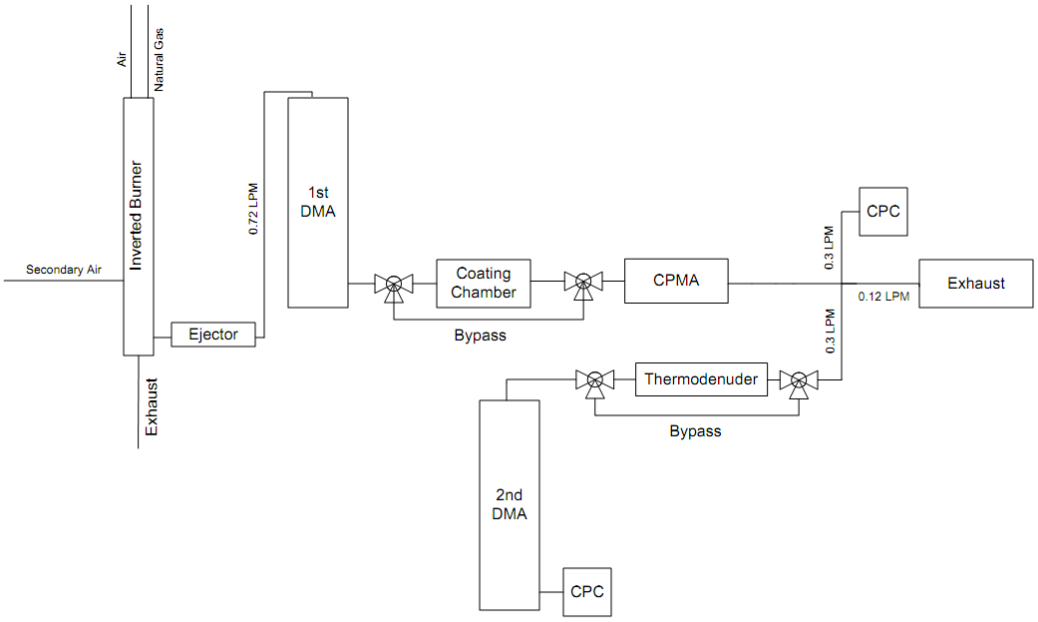

Figure 5.1. Schematic diagram of the experimental setup

5.2.1 Burner

An inverted co-flow diffusion flame based on the design of Stipe et al. (2005) was used to produce soot particles. This burner can produce a wide range of soot particles sizes and concentrations. Due to the inverted design, the buoyant gases from combustion flow downward which prevent the flame from flickering. Hence, the concentration and size distribution of generated soot is steady with respect to time. In addition, Kirchstetter and Novakov (2007) have shown using laser fragmentation-fluorescence spectroscopy that the soot particles generated by this burner have no measurable organic material on the particles. Our direct

measurement of the mass of soot particles by CPMA before and after passing through a thermodenuder at 200^{o}C confirms that there is not a measureable amount of volatile material on the generated soot.

Natural gas and air were supplied to the burner via mass flow controllers at flow rates of 1.3 SLPM (Cole-Parmer, model 32907-69) and 18 SLPM (Omega, model FMA-774-V), respectively. Primary dilution air, controlled by another mass flow controller (Omega, FMA-774-V), was injected into the exhaust at a flow rate of 37 SLPM. An ejector dilutor was used to dilute the sample by a further factor of 15.

5.2.2 Coating Chamber

Soot particles were coated with either oleic acid or dioctyl sebacate (DOS). The aerosol flow was passed through a coating chamber similar to the design of Moteki and Kondo (2007). The coating chamber is essentially a test tube (3 cm in diameter and 20 cm in length) partially filled with the coating material and maintained at constant temperature with an oil bath. The aerosol flow enters and exits the test tube through glass tubes passing through a stopper on top of the test tube. The bath temperature was held in the range of 95 to 100^{o}C and 112 to 117^{o}C for oleic acid and DOS coating respectively. As a result the maximum achieved mass fraction (the ratio of mass of the coating to the mass of the soot particle) of oleic acid and DOS coating for 350 nm particles were 10 and 8, respectively.

5.2.3 Differential Mobility Analyzer

The DMA classifies particles by their electrical mobility. Two DMAs were used in this study as shown in Figure 5.1. The first DMA contained a Kr-85 neutralizer and the particles were not re-neutralized in the second DMA. The first DMA was used to select a monodisperse aerosol from the polydisperse soot distribution exiting the burner. Particle size (core size) from 100 nm to 450 nm was selected. The second DMA was used in a scanning mode with a CPC to measure the diameter of soot particles after the thermodenuder.

In general, the ratio of sheath to aerosol flow rate was maintained at approximately 10, except when large particles were classified which required that a lower sheath flow rate be used. The aerosol flow rate through the first DMA and CPMA was maintained at 0.72 LPM. The sheath flow of the first DMA was 6 LPM for selecting particles with diameter of 450 nm and 7 LPM for other diameters. The sheath flow of the second DMA was maintained at 3 LPM. Both CPC measurements were operating at low flow rate mode (0.3 LPM). To minimize the effect of coagulation on the results, all bypass flow paths had the same residence time as the coating chamber or thermodenuder.

5.2.4 Centrifugal Particle Mass Analyzer

The centrifugal particle mass analyzer (CPMA) consists of two coaxial rotating cylinders. The inner cylinder is placed at a negative high voltage and the outer cylinder is at ground, thus positively charged particles are attracted to the inner cylinder. Therefore, these particles experience two different forces: electrostatic

force and centrifugal force. Since the directions of these forces are opposite, at a set voltage and speed, particles in a narrow ratio of mass-to-charge will exit the classifier. These principle of operation is similar to the aerosol particle mass analyzer (APM; Ehara et al., 1996), except the inner cylinder in the CPMA rotates slightly faster than the outer one, which increases the amplitude of the transfer function (Olfert et al., 2007). Similar to the DMA, by connecting the CPMA to a CPC, and stepping the voltage and speed, the mass distribution of polydisperse aerosol can be found. However when the inlet aerosol is monodisperse (like aerosol from the DMA), simply stepping the voltage at a set speed is sufficient to find the mass of particles, where:

$$m_c = \frac{neV_c}{\omega_c^2 r_c^2 \ln\left(\frac{r_2}{r_1}\right)} \tag{5.1}$$

where e is the electronic charge, n is the number of charges, V_c is the voltage at which the transfer function is maximum, $r_1$and $r_2$are the inner and outer radius of the cylinders, r_c is the average of r_1 and r_2, and ω_c is the angular velocity of the fluid at r_c.

5.2.5 Thermodenuder

The thermodenuder consist of a long piece of copper tubing with two parts: a heating section and a cooling section. The heating section was maintained at 200^{o}C and the cooling section was maintained at room temperature**.** Activated carbon was not used in the cooling section as it has been shown by Saleh et al. (2011), which should be avoided. To check the efficiency of the thermodenuder,

the mass of size-selected particles before coating and after the coating/denuding process are compared. The results show no change in mass, which means that the thermodenuder could efficiently take off the thick coatings from the soot particles.

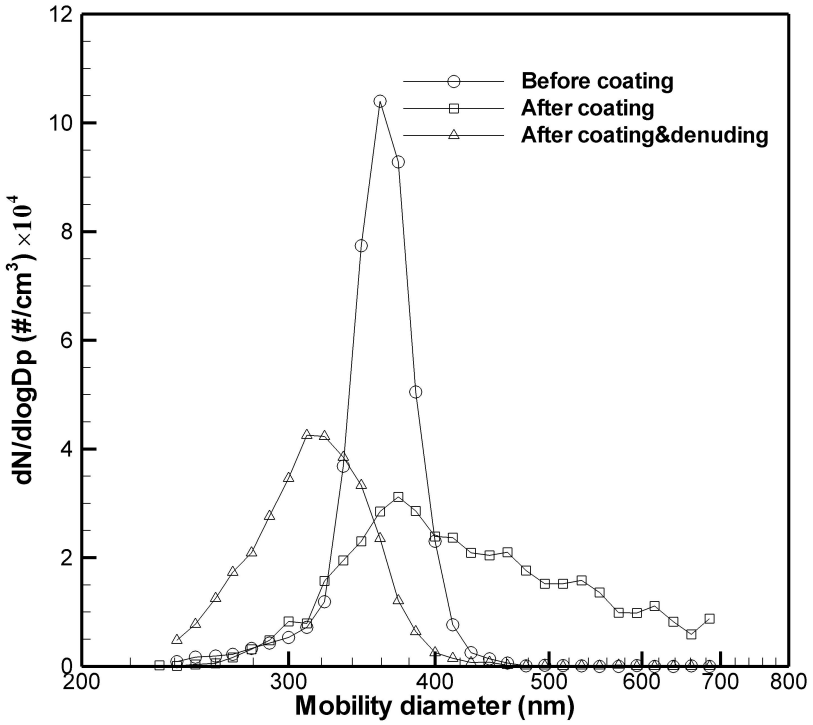

Figure 5.2. Size distribution of DMA-selected 350 nm soot particles before coating, after coating and after coating/denuding

5.3 Results and discussion

Figure 5.2 shows the size distributions of DMA-selected 350 nm soot particles before coating, after being coated with oleic acid and after being coated/denuded. The figure shows that coating with oleic acid makes the size distribution wider which is consistent with Moteki & Kondo (2007). This wide distribution after coating shows not all particles grow the same amount, some obtain substantial amounts of coating while other particles receive relatively little coating. Due to this different coating thickness, the amount of particle collapse is not the same for

all of the particles, which causes the denuded particle size distribution to become broader than the original particle distribution as shown in the figure. The novel point of this study is to study the effect these different coating thicknesses. After the coating process the amplitude of the size distribution decreased significantly as the distribution widened, but the total number concentration of particles only decreased by approximately 5%. This plot also shows that with coating the count mode diameter does not change considerably at this specific coating chamber temperature, initial diameter, and number of concentration. This behavior is due the fact that though the particles have been coated and the soot core has collapsed at the same time. However, with denuding the count mode diameter decreases from 359 nm (before coating) to 310 nm (after coating/denuding) because of a collapse of the particle core.

Fig 5.3 depicts the change in mobility diameter as a function of coating mass for undenuded soot. In Fig 5.3(a) the coating material is DOS and the initial mobility diameter of soot particles is 100, 150, 350 and 450 nm. In Fig 5.3(b) the initial mobility diameter is 250, 350 and 400 nm that are coated with oleic acid. The mass coating ratio (m_{coated}/m_0) and size coating ratio (d_{coated}/d_0) are defined as:

$$\frac{m_{coated}}{m_0} = \frac{\text{Total mass of black carbon and coating}}{\text{Mass of initial soot particle}} \tag{5.2}$$

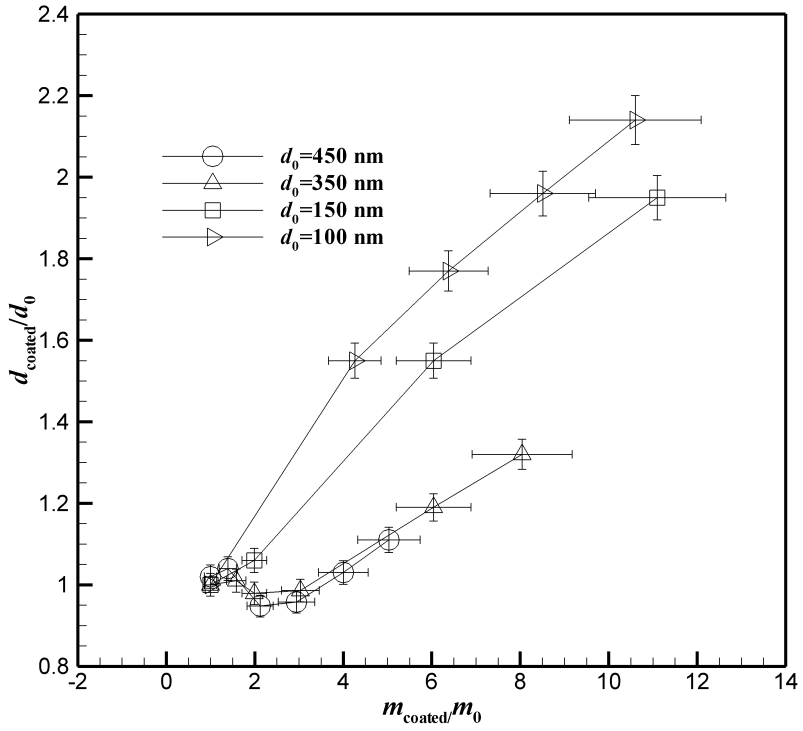

(a)

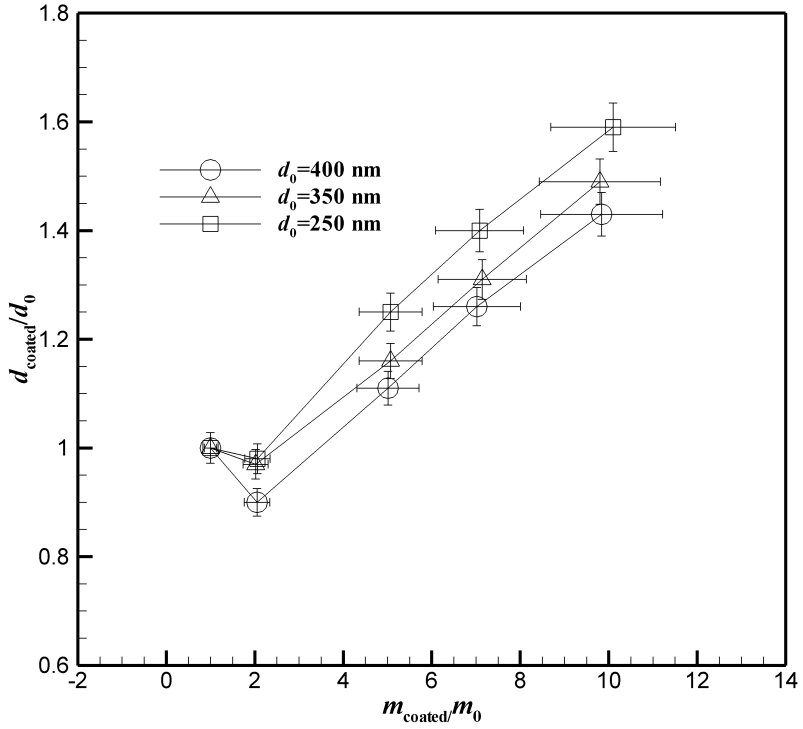

(b)

Figure 5.3. Change in mobility diameter as a function of coating mass for (a) DOS and (b) oleic acid

and

$$\frac{d_{\text{coated}}}{d_0} = \frac{\text{Mobility diameter of black carbon and coating}}{\text{Mobility diameter of initial soot particle}} \tag{5.3}$$

As previously mentioned since there is no volatile material on the soot particles generated from the inverted burner, so the terms “mass of the initial soot particles”, “mass of the fresh soot particles” and “mass of the black carbon core” all imply the same parameter.

The mass coating ratio ranges from 1 (no coating) to near 12 for the measurements shown in this work. As shown in Figure 5.2, a wide range of coating thickness is possible at a given condition, however, the number concentration decreases as the coating thickness becomes large. The maximum achievable mass coating ratio is limited by having an adequate number of particles counted by the CPC. As the initial diameter increases, the maximum achievable m_{coated}/m_0 for DOS coating decreases as shown in Fig 5.3. The higher coating ratios with DOS were not achieved because there were not a sufficient number of particles for reliable measurements. However, for coating with oleic acid, mass coating ratios of approximately 10 were obtained for all three initial particle sizes.

It can be seen from Fig 5.3 that at low mass coating ratios the mobility diameter can actually decrease even though coating material has been added to the particle. This trend can be attributed to the collapse of the soot particle when it is coated.

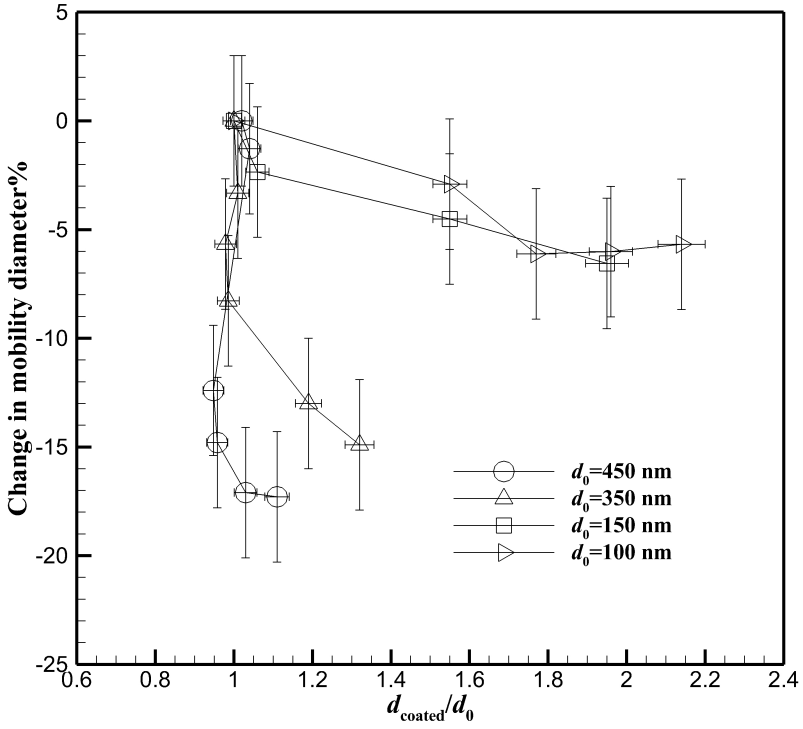

(a)

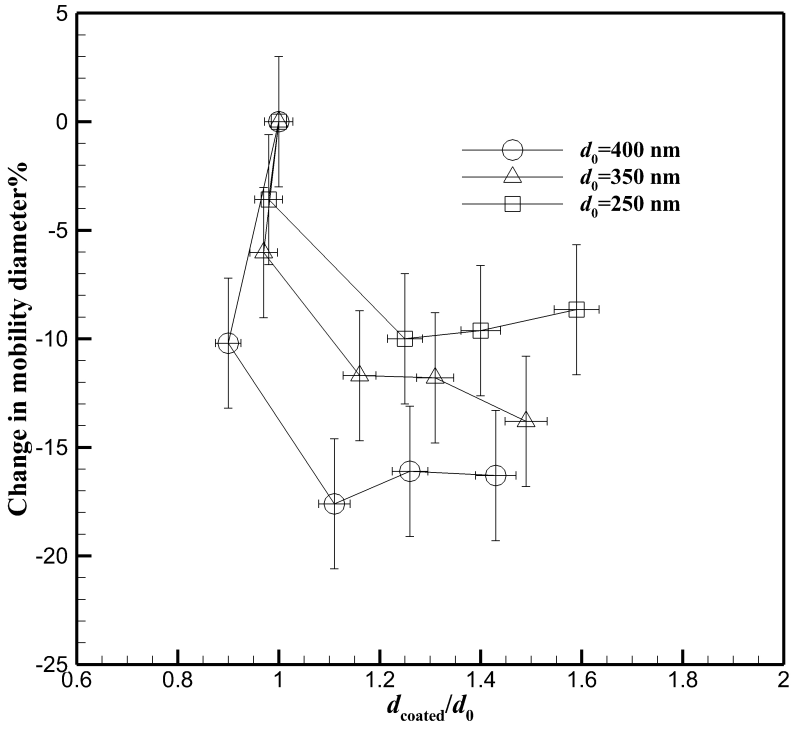

(b)

Figure 5.4. Change in mobility diameter after coating and denuding the soot particles for different coating thickness for (a) DOS (b) oleic acid coating

This decrease in mobility size tends to have the strongest effect on particles with a larger initial particle size and for coating mass ratios of approximately 2. At this mass coating ratio there is enough coating material to cause particle collapse, but not enough coating material to significantly increase the mobility of the particles. Figure 5.4 shows the change in mobility diameter after coating and denuding the soot particles for different coating mass factions. The percentage change in mobility diameter has been defined as:

$$\text{change in mobility diameter}\,(\%) = \frac{d_{\text{denuded}} - d_0}{d_0} \times 100 \qquad (5.4)$$

where d_{denuded} is the mobility diameter after the coating and denuding process. The horizontal axis of these graphs is d_{coated}/d_0, which is sometimes used in the literature. However, mobility measurements are a poor measure of the amount of coating on the particle since particle collapse can result in reductions in particle mobility as coating is added (i.e. leading to the false conclusion that the particles may collapse with very little coating thickness). A better method to quantify the amount of coating material on the soot particle is to use the mass ratio of coating material (m_{coated}/m_0), which is in dependent of particle shape, as showed in Figure 5.5. These plots show how soot particles collapse as the coating mass increases. As expected, large particles have a greater reduction in particle size due to collapse than small particles at the same coating mass fraction, since larger agglomerate soot particles will have a more open structure (i.e. a lower effective density, as seen below).

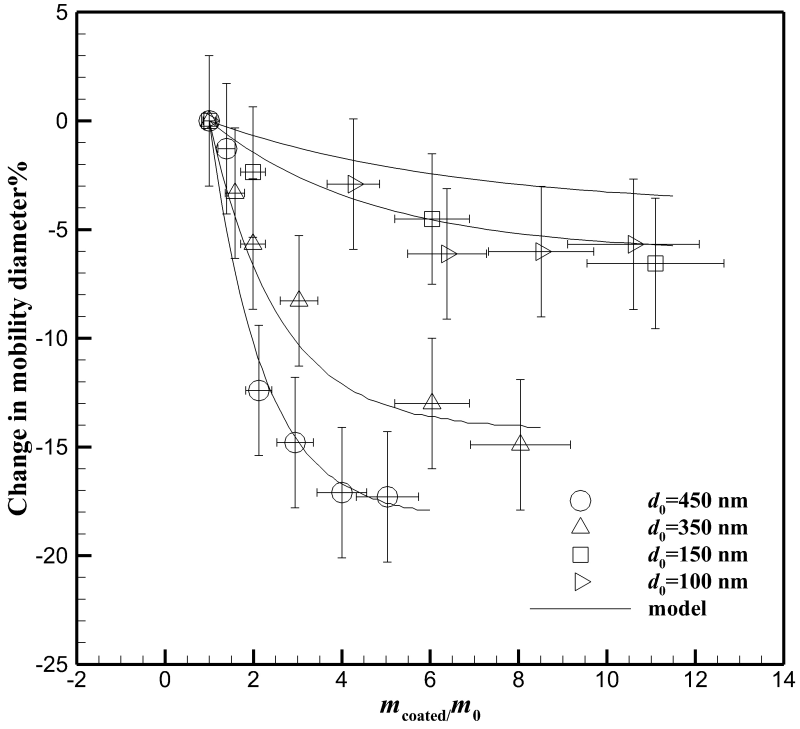

(a)

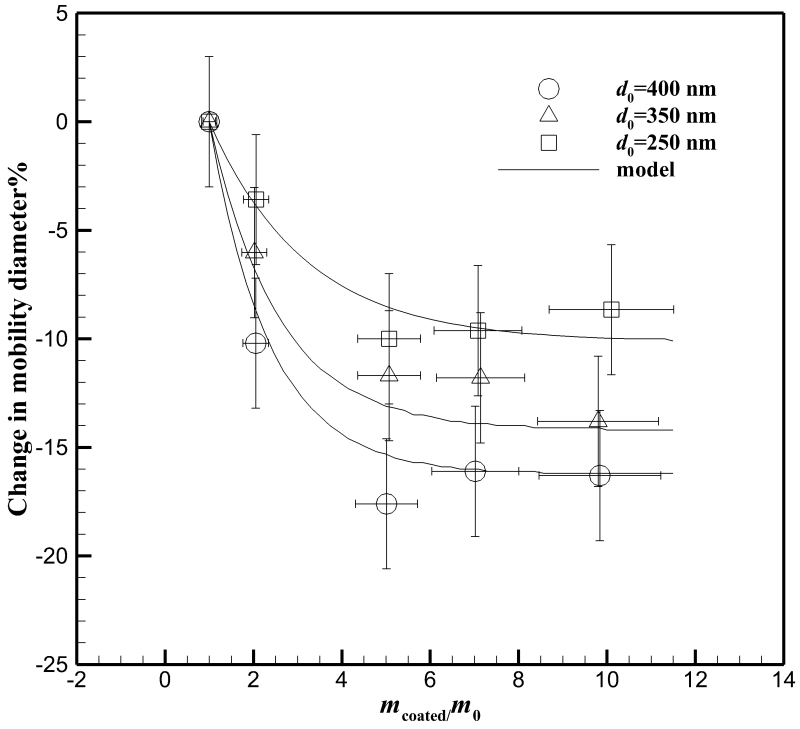

(b)

Figure 5.5. Change in mobility diameter after coating/denuding process as the coating mass increases for (a) DOS and (b) oleic acid coating

As seen in the figure 5.5, when the coating mass fraction becomes large (approximately 5 or greater for the results shown here), the degree of particle collapse becomes constant. It will be shown below that at mass fractions higher than approximately 5, the soot particle becomes completely encapsulated with coating (i.e. the dynamic shape factor is 1). Therefore, it is expected that higher amounts of coating will not further collapse the particle with this coating materials. In much of the literature (for example: Xue et al. , 2009b) the restructuring of soot particles is attributed to the surface tension of the coating liquid. Comparing the surface tension of oleic acid (32.79 mN/m; Chumpitaz et al., 1999) and DOS (31.73 mN/m; Wohlfarthand Wohlfarth, 1997), shows that the surface tension of these two material are quite similar. Thus for the same amount of coating mass, having the same degree of restructuring seems reasonable.

Slowik et al. (2007) qualitatively showed that the collapsing of soot particles by oleic acid is consistent with previous studies. Cross et al. (2010) coated particles with DOS and concluded that the DOS did not cause significant collapse. Cross et al. (2010) reached this conclusion based on the change in the mass-mobility exponent of the particles (the mass-mobility exponent of fresh soot was 2.12+/-0.04 and after the coating/denuding process the exponent was 2.17+/-0.06). Cross et al. (2010) did notice a small increase in the mass mobility exponent for DOS-coated/denuded soot (an increase in mass-mobility exponent implies that the particle became more spherical due to collapse), but the change was within the uncertainty of the measurement. However it can be seen from Figure 5.5(a) that a change in mobility diameter of the soot particles due to DOS coating can be more

than 15%. This difference in conclusion is likely due to the size range of soot particles tested and the degree of particle coating. The maximum diameter of the initial soot particle used by Cross et al. (2010) was approximately 250 nm. As shown in this work, small particle sizes (100 and 150 nm) have a very small change in particle size after collapsing and this small change may be difficult to measure.

A parameterization was developed to describe the change in mobility diameter as a function of initial core size and amount of coating mass. The model is shown with solid lines in Fig 5.5. This model maybe useful for climate modelers to calculate the change in the optical properties of atmospherically processed soot based of the amount of coating material and initial particle size. The model was based on a simple exponential decay:

$$\text{change in mobility diameter \%} = ad_0\,(1-\exp(bd_0\,(m_{\text{coated}}/m_0\,-1)) \qquad (5.5)$$

where a and b are constants. The term bd_0 is analogous to the inverse of the time constant in a first-order system. The term ad_0 is simply the maximum change in the initial mobility diameter (in percent). By employing the method of least squares, the constants were determined to be a=-0.0405 $nm^{-1}$and b=–0.0018 $nm^{-1,}$ with a coefficient of determination of R^2=0.97. Note that the same coefficients are used for both DOS and oleic acid.

Figure 5.6 compares the model calculations with the experimental data. Good agreement is seen for particles larger than 100 nm but the model underestimates

the collapsing of 100 nm particles (see Figure 5.5(a)). A better fit could be obtained by replacing coefficient *a* with a high order polynomial to account for this underestimation at 100 nm, however, this is not physically justified, since very small particles (those containing just a few primary particles) cannot not collapse

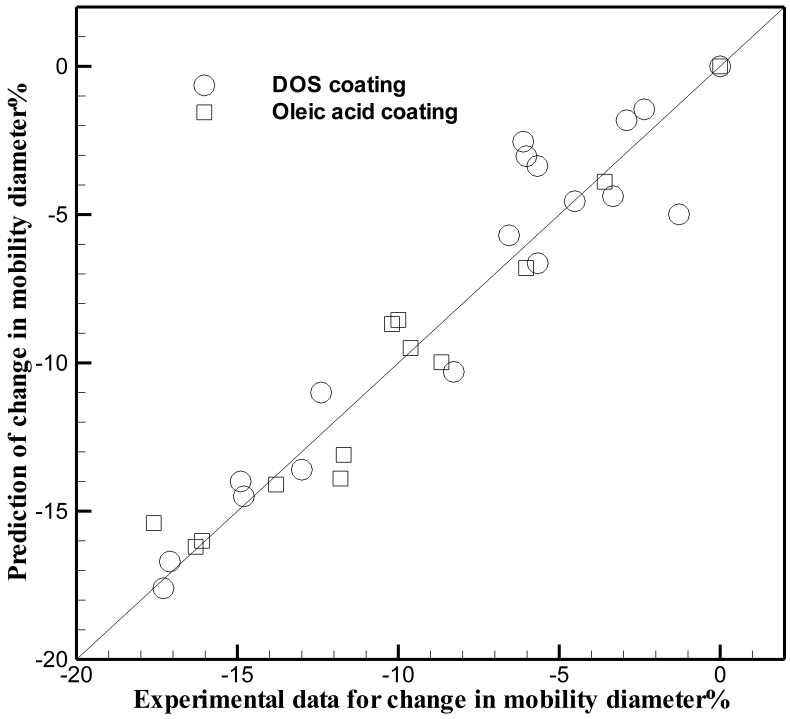

Figure 5.6. Comparing model predication of change in mobility diameter with the experimental results

by coating. A more reasonable solution is using a piecewise function, but more experimental points with small initial diameters are needed.

The effective density of a particle has an important role in particle transport properties. It is also required for calculating mass size distributions from mobility size distributions and finding the relationship between mobility diameter and aerodynamic diameter (Park et al. 2003). When particles are spherical without any

internal voids the density of a particle can be calculated by knowing the mass of and diameter of the particle. When particles are not spherical, like soot particles, another diameter such as mobility equivalent diameter (d_{me}) can be used. This equivalent diameter may be used to calculate "effective" or "apparent" density (DeCarlo et al., 2004), which will be lower than the material particle density. The effective density is defined as :

$$\rho_{eff} = \frac{m}{\frac{\pi}{6} d_{me}^3} \tag{5.6}$$

McMurry et al. (2002) used a DMA and APM to measure effective density and the same technique has been employed for a DMA-CPMA system (Olfert et al., 2007).

The method for determining the effective density of the particles differed depending on whether the particles were coated or not. For coated particles, particles were classified by their size through the first DMA, coated, classified by their mass by setting CPMA at specific voltage and speed and then scanned by the seconded DMA to find their mobility size. Hence their mass and their mobility size are known for finding effective density. For uncoated particles, the CPMA was set at a specific speed and CPMA voltage was stepped to find the initial mass of particles. Then the CPMA was set to the voltage at which the transfer function of the CPMA was a maximum and the particle size was measured by the second DMA. The effective density of coated particles as a function of mass coating ratio is shown in Fig 5.7 for DOS and oleic acid.

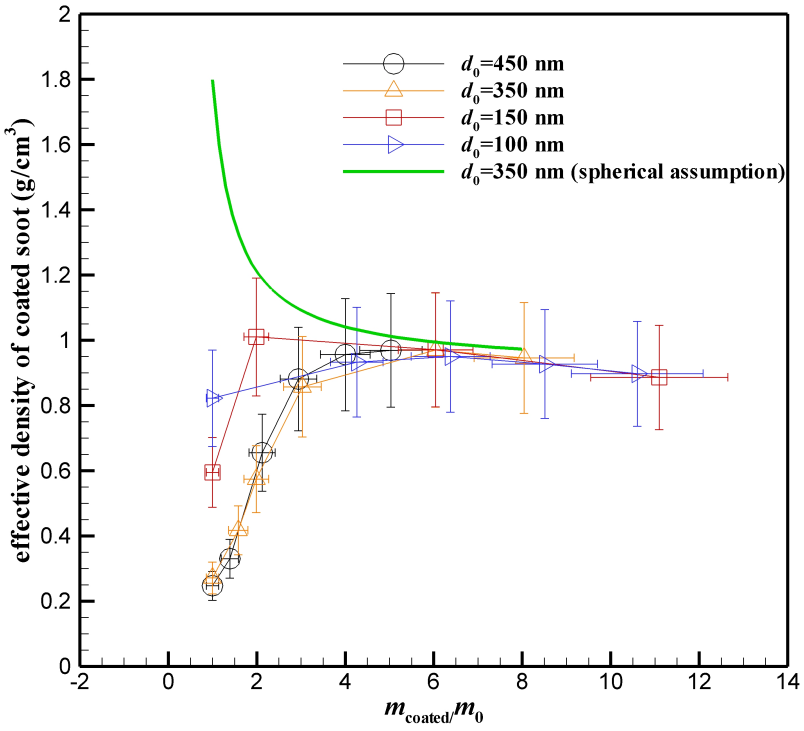

(a)

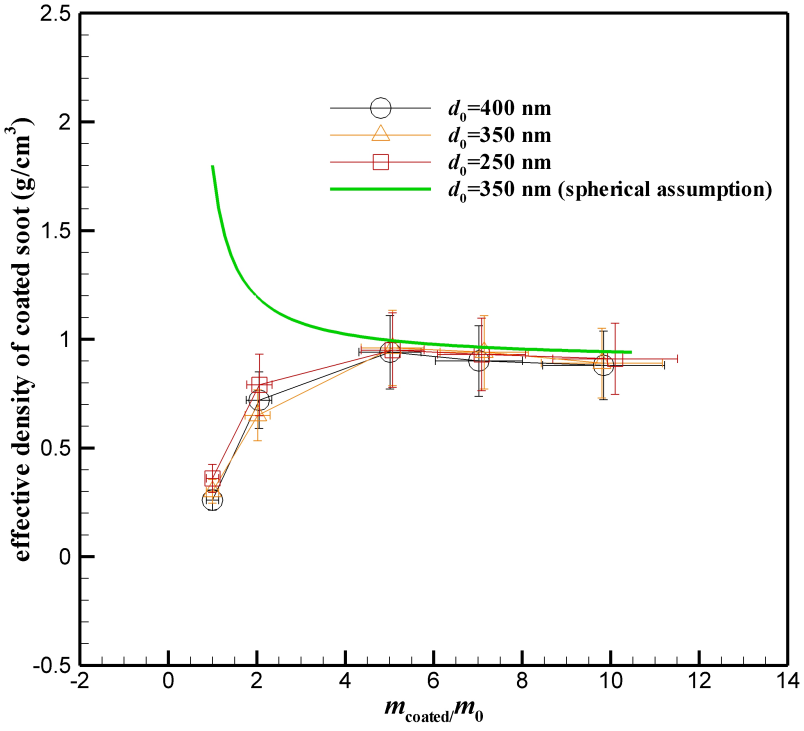

(b)

Figure 5.7. The effective density of coated particles as a function mass coating ratio for (a) DOS and (b) oleic acid coatings

With increasing coating mass the effective density initially increases and then starts to decrease as more coating material is added. This can be explained by the fact that although the material density of soot particles is 1.8 g/cm^3, the effective density of the soot particles are between 0.3 to 0.8 g/cm^3 depending on their initial size. Hence when the coating condenses on the soot, the density increases because the mass increases but the mobility diameter does not increase significantly for small amount of coating as shown in Fig 5.3. In fact, the small amount of coating may cause the particles to collapse, which further increases the effective density .As the coating increases, particles get closer to a spherical shape and the effective density increases. With thicker coatings, the mass fraction of coating increases and due the fact the coating material density (0.9 g/cm^3) is lower than the material density of soot (1.8 g/cm^3) the effective density decreases. The material density and the mass of the carbon and the coating materials are known, the theoretical density of coating can be calculated. The theoretical material density of 350 nm particles for different coating mass factions is plotted with the assumption of spherical particles. As coating mass increases and the particles get more spherical shape, the experimental effective density approaches the theoretical density.

In Fig 5.8 the effective density of denuded soot particles for different mass coating ratios are shown. It can be seen that the effective density of the initial soot particles ranged from 0.2 to 0.8 g/cm^3, with smaller densities for larger initial particle sizes. After coating and denuding the effective density increases due to particle collapsing.

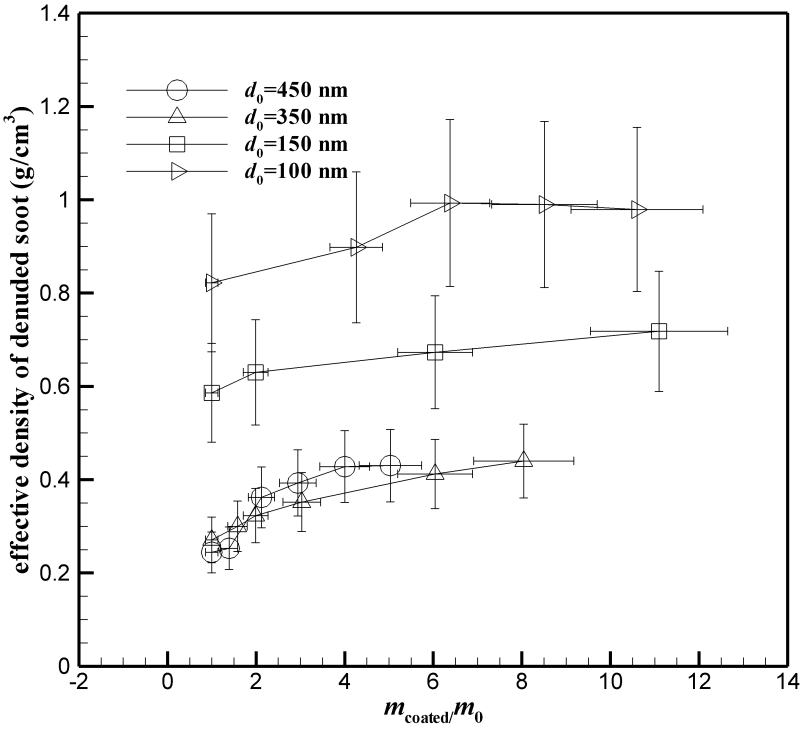

(a)

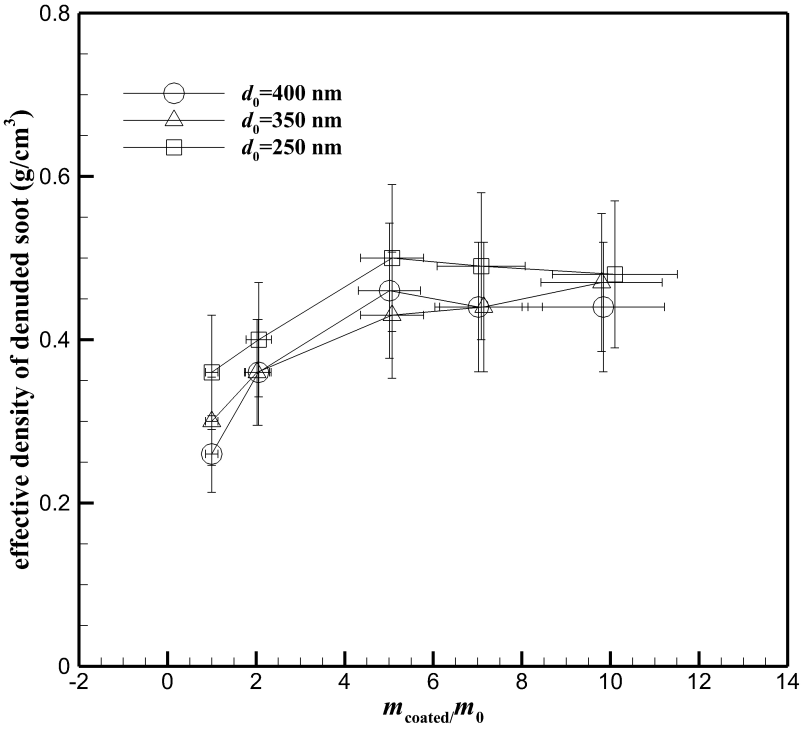

(b)

Figure 5.8. The effective density of coated/denuded particles as a function mass coating ratio for (a) DOS and (b) oleic acid coatings

It can be seen from this figure that for m_{coated}/m_0 approximately greater than five, the density does not considerably change, which means (as mentioned before) the collapsing is effectively complete once m_{coated}/m_0 more than five.

Another important particle property is the dynamic shape factor, which is shown in Fig 5.9, for the DOS and oleic acid coated soot. The dynamic shape factor is defined as the ratio of the actual drag force on a particle to the drag force on a spherical particle with the same volume (including any internal voids in the particle). It is obvious from the definition that for spherical parties the shape factor is 1 (Hinds, 1999). For nonspherical particles this value is usually greater than 1. The dynamic shape factor has been calculated using the expression from (Hinds, 1999):

$$\chi = \frac{d_{me}}{d_{ve}} \frac{C_{ve}}{C_{me}} \tag{5.7}$$

where d_{ve} is the volume equivalent diameter, d_{me} is mobility diameter, and C_{ve} and C_{me} are respectively the corresponding slip correction factors.

Figure 5.9 show that for initial soot particles the shape factor ranges from 1.5 to 2.5 as diameter increases from 100 nm to 450 nm. The shape factor of coated particles is designated with solid symbols. Condensing coating material on the soot causes the shape factor to drastically decrease to one and become constant for a mass coating ratios approximately greater than 5. The figure shows that when particles are coated they become spherical independent of their initial size, which is in agreement with density results as discussed above.

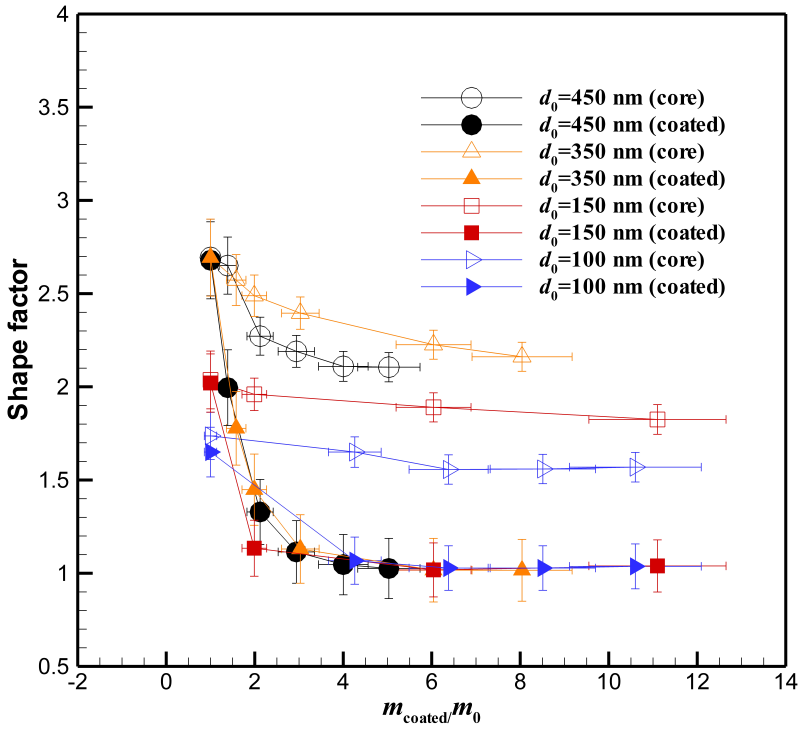

(a)

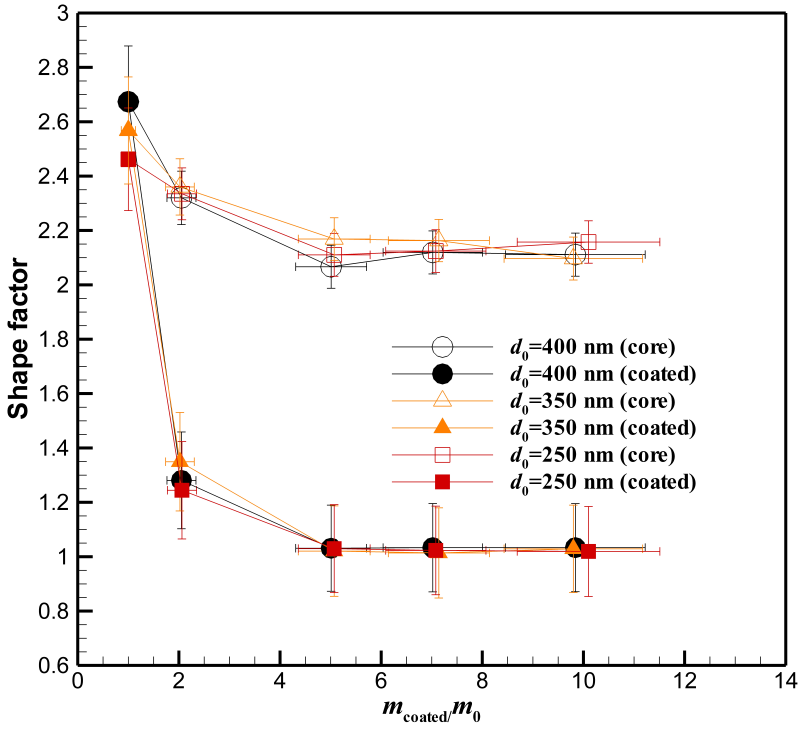

(b)

Figure 5.9. The dynamics shape factor as a function mass coating ratio for (a) DOS and (b) oleic acid coatings

Another observation from graphs is that with coating and denuding process the shape factor decreases as expected. The figure also shows that the particles do not completely collapse until the particles are completely coated.

The particle mass-mobility relationship before coating with oleic acid, after coating, and after coating/denuding is shown in Fig. 5.10 for particles that were coated with the highest mass ratio. It has been shown that the relation between mass and mobility diameter can be described by (Park et al., 2003):

$$m = Cd_{\mathrm{m}}^{D_{\mathrm{fm}}} \tag{5.8}$$

where C is a constant and D_{fm} is mass-mobility exponent (which is sometimes referred to as the mass fractal dimension (Kim et al., 2009)). The solid lines in Figure 5.10 are a fit of the data using Equation (5.8). The results indicate that upon coating with oleic acid, the mass-mobility exponent increases from 2.14±0.03 to 3.02±0.05 (for the highest mass fraction of coating) because with coating the particles become spherical in shape. After denuding, the mass-mobility exponent decreases to 2.38±0.06, which is still higher than the mass-mobility exponent of fresh soot. This increase in the mass-mobility exponent is due to the restructuring of soot particles. The fact that after denuding the D_{fm} is less than 3, shows that particles are not spherical after coating/denuding and further collapse might be possible. For example, Cross et al. (2010) reported that by coating with sulfuric acid and denuding soot particles with mass-mobility exponent of 2.12±0.04, the mass-mobility exponent increased to 2.49±0.07. The higher mass-mobility exponent reported by Cross et al. (2010) could be due to the

fact that the surface tension of sulfuric acid (52.55mN/m; Wohlfarthand Wohlfarth, 1997) is greater than oleic acid (32.79 mN/m; Chumpitaz et al., 1999), or perhaps the structure of the soot itself (i.e. primary particle size) may have allowed for a higher degree of collapse.

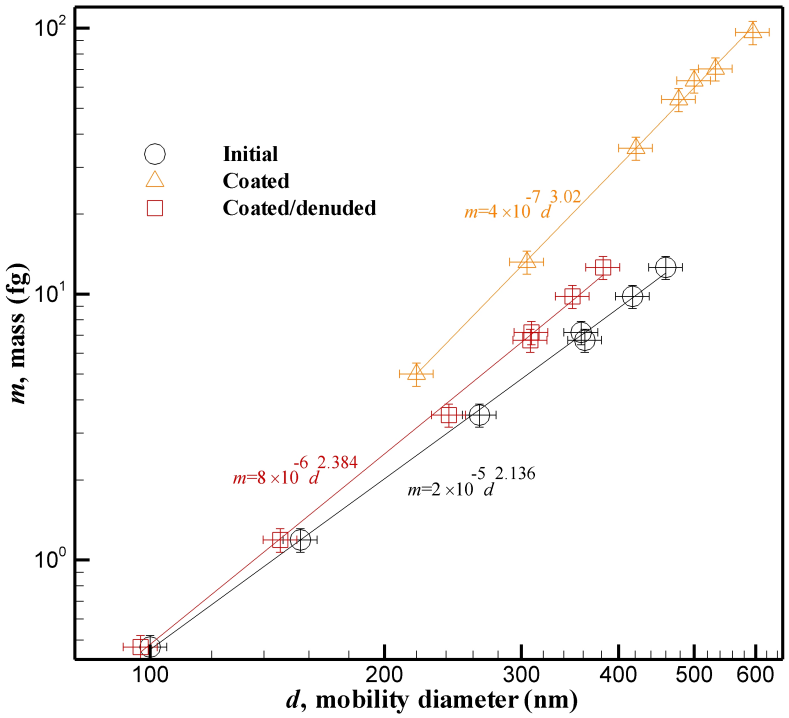

Figure 5.10. The particle mass-mobility relationship before coating, after coating with oleic acid (with the highest mass ratio), and after coating/denuding

5.4 Conclusions

Soot particles in the atmosphere have different amounts of coating, and the morphology and optical properties of soot can change depending on the coating thickness. In this study, the effect of coating thickness on the morphology of soot particles was investigated using oleic acid and DOS coatings. A wide range of coating thicknesses was used, with up to 12 times as much coating as the mass of the soot. It was shown that as the coating mass increases the degree of collapsing

increases, but after the mass coating fraction becomes approximately greater than 5, the change in diameter of the BC core is not significant. A model was presented to predict the change in mobility diameter as a function of coating mass ratio. This model can be improved by further measurement of smaller particles and other coating materials. The change of effective density of soot particles in coating/denuding process was reported. As the coating mass increases the effective density drastically increases and as more coating is placed on the particle it gradually decreases. After denuding the coated particles, the effective density increases due to particle collapsing.

Condensing coating material on the soot causes the shape factor to drastically decrease to one and become constant for a mass coating ratio approximately greater than 5. After the coating/denuding process the shape factor decreases compared to fresh particles. Upon coating, the mass-mobility exponent increases from 2.14±0.03 to 3.02±0.05 for the highest mass fraction of coating and after denuding decreases to 2.38±0.06.

5.5 References

Chumpitaz, L.D.A., Coutinho, L.F., Meirelles, A.J.A., 1999. Surface tension of fatty acids and triglycerides. *Journal of the American Oil Chemists' Society* 76, 379-382.

Cross, E., Onasch, T., Ahern, A., Wrobel, W., Slowik, J.G., Olfert, J., Lack, D., Massoli, P., Cappa, C., Schwarz, J., Spackman, J.R., Fahey, D., Sedlacek, A., Trimborn, A., Jayne, J., Freedman, A., Williams, L., Ng, N., Mazzoleni, C., Dubey, M., Brem, B., Kok, G., Subramanian, R., Freitag, S., Clarke, A., Thornhill, D., Marr, L., Kolb, C., Worsnop, D., Davidovits, P., 2010. Soot particle studies—instrument inter-comparison—project overview. *Aerosol Science and Technology* 44, 592-611.

DeCarlo, P., Slowik, J.G., Worsnop, D., Davidovits, P., Jimenez, J., 2004. Particle morphology and density characterization by combined mobility and aerodynamic diameter measurements. part 1: Theory. *Aerosol Science and Technology* 38, 1185-1205.

Ehara, K., Hagwood, C., Coakley, K.J., 1996. Novel method to classify aerosol particles according to their mass-to-charge ratio-aerosol particle mass analyser. *Journal of Aerosol Science* 27, 217-234.

Hinds, W.C., 1999. Aerosol technology—properties, behavior, and measurement of airborne particles., 2nd ed. John Wiley & Sons, New York, New York.

Jacobson, M.Z., 2001. Strong radiative heating due to the mixing state of black carbon in atmospheric aerosols. *Nature* 409, 695-697.

Kim, S.C., Wang, J., Emery, M.S., Shin, W.G., Mulholland, G.W., Pui, D.Y.H., 2009. Structural property effect of nanoparticle agglomerates on particle penetration through fibrous filter. *Aerosol Science and Technology* 43, 344-355.

Kirchstetter, T.W., Novakov, T., 2007. Controlled generation of black carbon particles from a diffusion flame and applications in evaluating black carbon measurement methods. *Atmospheric Environment* 41, 1874-1888.

McMeeking, G.R., Good, N., Petters, M.D., McFiggans, G., Coe, H., 2011. Influences on the fraction of hydrophobic and hydrophilic black carbon in the atmosphere. *Atmospheric Chemistry and Physics II*, 5099-5112.

McMurry, P.H., Wang, X., Park, K., Ehara, K., 2002. Relationship between Mass and Mobility for Atmospheric Particles. *Aerosol Science and Technology* 36, 227-238.

Moteki, N., Kondo, Y., 2007. Effects of mixing state on black carbon measurements by laser-induced incandescence. *Aerosol Science and Technology* 41, 398-417.

Olfert, J.S., Symonds, J.P.R., Collings, N., 2007. The effective density and fractal dimension of particles emitted from a light-duty diesel vehicle with a diesel oxidation catalyst. *Journal of Aerosol Science* 38, 69 - 82.

Pagels, J., Khalizov, A., McMurry, P., Zhang, R., 2009. Processing of Soot by Controlled Sulphuric Acid and Water Condensation—Mass and Mobility Relationship. *Aerosol Science and Technology* 43, 629-640.

Park, K., Cao, F., Kittelson, D.B., McMurry, P.H., 2003. Relationship between particle mass and mobility for diesel exhaust particles. *Environmental Science & Technology* 37, 577-83.

Saleh, R., Shihadeh, A., Khlystov, A., 2011. On transport phenomena and equilibration time scales in thermodenuders. *Atmospheric Measurement Techniques* 4, 571-581.

Shiraiwa, M., Kondo, Y., Moteki, N., Takegawa, N., Miyazaki, Y., Blake, D.R., 2007. Evolution of mixing state of black carbon in polluted air from Tokyo. *Geophysical Research Letters* 34, 2-6.

Slowik, J.G., Cross, E.S., Han, J.-H., Kolucki, J., Davidovits, P., Williams, L.R., Onasch, T.B., Jayne, J.T., Kolb, C.E., Worsnop, D.R., 2007. Measurements of Morphology Changes of Fractal Soot Particles using Coating and Denuding Experiments: Implications for Optical Absorption and Atmospheric Lifetime. *Aerosol Science and Technology* 41, 734-750.

Stipe, C., Higgins, B., Lucasa, D., Koshland, C., Sawyer, R., 2005. Inverted co-flow diffusion flame for producing soot. *Review of Scientific Instruments* 76, 023 908.

Wohlfarth, C., Wohlfarth, B., 1997. Surface tension of pure liquids and binary liquid mixtures, Group. Springers.

Xue, H., Khalizov, A.F., Wang, L., Zheng, J., Zhang, R., 2009a. Effects of dicarboxylic acid coating on the optical properties of soot. *Physical Chemistry Chemical Physics II*, 7869-7875.

Xue, H., Khalizov, A.F., Wang, L., Zheng, J., Zhang, R., 2009b. Effects of coating of dicarboxylic acids on the mass-mobility relationship of soot particles. *Environmental Science & Technology* 43, 2787-2792.

Zhang, R., Khalizov, A.F., Pagels, J., Zhang, D., Xue, H., McMurry, P.H., 2008. Variability in morphology, hygroscopicity, and optical properties of soot aerosols during atmospheric processing. *Environmental Sciences* 105, 10291- 10296.

Chapter 6: Conclusions and future work

6.1 Conclusions

It is generally accepted that aerosols can affect climate and Earth's temperature by the scattering and absorption of sunlight. Freshly emitted soot particles are typically hydrophobic and fractal, and mostly externally mixed with non-refractory compounds. The aging process can change the morphology and optical properties of soot particles. For fresh soot the absorption coefficient is greater than scattering coefficient. Therefore, the single scattering albedo is small (0.09 for example) but coating can increase the albedo. Soot particles in the atmosphere have different amounts of coating, and the morphology and optical properties of soot can change depend on coating thickness.

In the first part of this study the properties of soot particles generated from a inverted burner and a McKenna burner at different flow settings were compared. The size distribution, mass distribution, volatile mass fraction, effective density, mass concentration and mass-mobility exponent of particles from the inverted burner and the McKenna burner were measured. It was shown although there is no measureable amount of volatile material on the soot particles generated from the inverted burner, the soot generated from the McKenna burner could be have a mass of volatile material up to 5 times the mass of the non-volatile core particle. Data provided to select an appropriate burner and flow settings for particular applications. The mass-mobility exponent for soot particles generated by inverted burner ranges from 2.23 to 2.54 over a range of equivalence ratio of 0.55 to 0.69.

For the McKenna burner the mass-mobility exponent of generated soot ranges from 2.19 to 2.99 for fresh soot and 2.19 to 2.81 for denuded soot over a range of equivalence ratio of 2 to 3.75.

In the second part of the study, the effect of coating thickness on the morphology of soot particles from the inverted burners was investigated. A wide range of oleic acid and dioctyl sebacate coating thicknesses was used, with up to 12 times as much coating as the mass of the soot. It was shown that as the coating mass increases the degree of collapsing increases. A model was presented to predict the change in mobility diameter after the coating/denuding process. The change of effective density of soot particles in coating/denuding processes was reported. As the coating mass increases the effective density drastically increases and after that it slightly decreases. After denuding the coated particles, the effective density increases due to particle collapsing. Condensing coating material on the soot causes the shape factor to drastically decrease to one and become constant for a mass coating ratio of five. After a coating/denuding process the shape factor decreases compared to fresh particle. Coating increased the mass-mobility exponent from 2.14 to 3.02 (for the highest mass coating fraction)but after denuding mass-mobility exponent decreased to 2.38.

6.2 Future work

The model that was presented for collapsing the soot particles upon the coating process based on two different coating materials. As mentioned before more experimental points with small initial diameters (less than 100 nm) are needed to

predict the amount of collapsing for the broader range of diameters. The effect of other coating materials with different surface tensions can be investigated and the model can be improved for other coating materials. On the other hand the morphology of the fresh soot is also an important parameter that can change the degree of collapsing. Therefore soot from different sources and with different fractal dimensions can be used to quantify the effect of fresh soot properties on the collapsing.

Appendix A: Uncertainty Analysis

According to ANSI/ISA-S51.1the difference between the indication and the value of measured signal is called error. Since the value of “error” is not known this value should be estimated by uncertainty, which is the estimate of the error with a given confidence interval.

Two types of uncertainly can be defined "systematic" uncertainty (alternatively called bias uncertainty or "instrument" uncertainty), denoted by B_x, and the precision uncertainty (or "repeatability" uncertainty), denoted by P_x. While the precision uncertainty can be estimated from the data, the bias error is the inability of the equipment to measure the correct value it cannot be determined by repeating the measurement. The total uncertainty, U_x can be calculated by:

$$U_x = \sqrt{\sum B_x^2 + P_x^2} \tag{A-1}$$

Usually the bias uncertainty of the equipment is reported in its specification. The precision uncertainty can be calculated b:

$$P_x = t_{\frac{\alpha}{2},v} \frac{S_x}{\sqrt{n}} \tag{A-2}$$

Where $\alpha = 1 - c$, c is confidence, which is usually 95%, $\upsilon = n - 1$, S_x is the standard deviation of the measurements, and n is the number of measurements taken.

Using Propagation of Uncertainty methods, one can estimate the uncertainty in a variable from the known uncertainties in other variable. For example to calculate uncertainty in $y = y(x_1, x_2, ..., x_n)$, one can use the following equation:

$$\varepsilon_y^2 = \sum_{i=1}^{n} \left(\frac{\partial y}{\partial x_i} \right)^2 \varepsilon_i^2 \tag{A-3}$$

For purely multiplicative equation such as:

$$Q = A_1 F^a G^b H^c \tag{A-4}$$

The uncertainly can be easily found be:

$$\frac{dQ}{Q} = a\frac{dF}{F} + b\frac{dG}{G} + c\frac{dH}{H} \tag{A-5}$$

Table (A-1) has been used for calculating uncertainties.

Table (A-1).Uncertainties for equipment

Air flow rate for the inverted burner	Omega flow controller, model FMA-774-V	-1% full scale
Fuel flow rate for the inverted burner	Cole-Parmer flow controller model 32907-69	± 0.8% of Reading ±0.2% of Full Scale
Air flow rate for the McKenna burner	Cole-Parmer flow controller model 32907-71	± 0.8% of Reading ±0.2% of Full Scale
Fuel flow rate for the McKenna burner	Cole-Parmer flow controller model 32907-69	± 0.8% of Reading ±0.2% of Full Scale
Mass of the particles	CPMA	10%
Mobility diameter of particles	DMA	5%

For example the percentage of bias uncertainty for m_{coated}/m_0 in chapter 5 can be calculated by:

$$\left[(\frac{\varepsilon m_{\text{coated}}}{m_{\text{coated}}})^2 + (\frac{\varepsilon m_{\text{core}}}{m_{\text{core}}})^2\right]^{1/2} = \left((0.1)^2 + (0.1)^2\right)^{1/2} = 0.14 \qquad \text{(A-6)}$$

Therefore the uncertainty of m_{coated}/m_0 is 14%. The same procedure shows that uncertainty of d_{coated}/d_0 is 7%.

For the effective density one can see that

$$\rho = \frac{6m}{\pi d^3} \qquad \text{(A-7)}$$

Then:

$$\frac{\varepsilon_\rho}{\rho} = \left[(\frac{\varepsilon_m}{m})^2 + 9(\frac{\varepsilon_d}{d})^2\right]^{1/2} = \left[(0.1)^2 + 9(0.05)^2\right]^{1/2} = 0.18 \qquad \text{(A-8)}$$

Appendix B: Raw data

Table (B-1).Collected date from the McKenna burner

Equilalance ratio	dm (nm)	dm fresh (nm)	dm core (nm)	mass fresh (fg)	mass core (fg)	delta d (nm)	delta m (fg)	density (fresh) (gr/cm^3)	density (core) (gr/cm^3)
2	5.00E+01	4.92E+01	4.33E+01	7.76E-02	5.30E-02	1.36E+01	3.15E-01	1.24E+00	1.25E+00
2	7.50E+01	7.42E+01	6.85E+01	2.07E-01	1.59E-01	8.31E+00	2.30E-01	9.69E-01	9.47E-01
2	1.00E+02	9.85E+01	9.22E+01	3.91E-01	2.93E-01	6.84E+00	2.50E-01	7.81E-01	7.14E-01
2	1.50E+02	1.47E+02	1.40E+02	9.30E-01	7.40E-01	5.13E+00	2.04E-01	5.56E-01	5.14E-01
2	2.00E+02	1.95E+02	1.87E+02	1.77E+00	1.43E+00	4.02E+00	1.94E-01	4.58E-01	4.16E-01
2	2.50E+02	2.42E+02	2.30E+02	2.74E+00	2.26E+00	5.21E+00	1.75E-01	3.68E-01	3.53E-01
2	3.00E+02	2.88E+02	2.75E+02	3.89E+00	3.09E+00	4.74E+00	2.07E-01	3.11E-01	2.84E-01
2	3.50E+02	3.33E+02	3.16E+02	5.13E+00	4.22E+00	5.32E+00	1.78E-01	2.66E-01	2.56E-01
2.5	5.00E+01	4.95E+01	3.51E+01	9.19E-02	4.33E-02	4.11E+01	5.29E-01	1.45E+00	1.92E+00
2.5	7.50E+01	7.36E+01	6.37E+01	2.67E-01	1.63E-01	1.57E+01	3.90E-01	1.28E+00	1.21E+00
2.5	1.00E+02	9.84E+01	9.36E+01	5.62E-01	3.87E-01	5.10E+00	3.12E-01	1.13E+00	9.02E-01
2.5	1.50E+02	1.47E+02	1.43E+02	1.29E+00	9.80E-01	3.39E+00	2.38E-01	7.69E-01	6.47E-01
2.5	2.00E+02	1.95E+02	1.89E+02	2.46E+00	1.91E+00	3.05E+00	2.22E-01	6.35E-01	5.41E-01
2.5	2.50E+02	2.42E+02	2.34E+02	3.84E+00	3.14E+00	3.74E+00	1.82E-01	5.16E-01	4.71E-01
2.5	3.00E+02	2.90E+02	2.80E+02	5.45E+00	4.43E+00	3.81E+00	1.87E-01	4.25E-01	3.87E-01
3.1	5.00E+01	4.93E+01	2.76E+01	8.43E-02	2.30E-02	7.88E+01	7.27E-01	1.34E+00	2.09E+00
3.1	7.50E+01	7.37E+01	4.68E+01	2.42E-01	7.87E-02	5.75E+01	6.75E-01	1.15E+00	1.46E+00
3.1	1.00E+02	9.81E+01	6.63E+01	5.73E-01	2.19E-01	4.79E+01	6.17E-01	1.16E+00	1.44E+00
3.1	1.50E+02	1.47E+02	1.32E+02	2.01E+00	1.13E+00	1.17E+01	4.36E-01	1.21E+00	9.49E-01
3.1	2.00E+02	1.95E+02	1.83E+02	4.37E+00	2.81E+00	6.86E+00	3.58E-01	1.13E+00	8.82E-01
3.1	2.50E+02	2.43E+02	2.27E+02	7.41E+00	4.85E+00	6.79E+00	3.46E-01	9.89E-01	7.87E-01
3.1	3.00E+02	2.89E+02	2.71E+02	1.04E+01	7.40E+00	6.56E+00	2.86E-01	8.22E-01	7.10E-01
3.75	5.00E+01	5.06E+01	2.43E+01	8.06E-02	1.37E-02	1.09E+02	8.30E-01	1.19E+00	1.83E+00
3.75	7.50E+01	7.25E+01	4.01E+01	2.42E-01	4.18E-02	8.11E+01	8.27E-01	1.21E+00	1.24E+00
3.75	1.00E+02	9.83E+01	5.38E+01	5.28E-01	1.07E-01	8.27E+01	7.98E-01	1.06E+00	1.31E+00
3.75	1.50E+02	1.46E+02	8.15E+01	1.84E+00	3.56E-01	7.96E+01	8.07E-01	1.12E+00	1.25E+00
3.75	2.00E+02	1.94E+02	1.08E+02	4.42E+00	8.16E-01	7.93E+01	8.15E-01	1.15E+00	1.22E+00
3.75	2.50E+02	2.39E+02	1.30E+02	8.22E+00	1.42E+00	8.42E+01	8.28E-01	1.15E+00	1.24E+00

Table (B-2). Collected date from the inverted burner

Equilalance ratio	dm (nm)	mass (fg)	density (gr/cm^3)
0.55	5.00E+01	4.80E-02	7.29E-01
0.55	7.00E+01	1.04E-01	5.79E-01
0.55	1.00E+02	2.25E-01	4.29E-01
0.55	1.50E+02	5.48E-01	3.10E-01
0.55	2.00E+02	1.08E+00	2.57E-01
0.56	5.00E+01	4.94E-02	7.55E-01
0.56	7.00E+01	1.04E-01	5.81E-01
0.56	1.00E+02	2.28E-01	4.36E-01
0.56	1.50E+02	5.54E-01	3.13E-01
0.56	2.00E+02	1.11E+00	2.64E-01
0.56	3.00E+02	2.52E+00	1.78E-01
0.57	5.00E+01	5.07E-02	7.75E-01
0.57	7.00E+01	1.07E-01	5.95E-01
0.57	1.00E+02	2.36E-01	4.50E-01
0.57	1.50E+02	5.70E-01	3.22E-01
0.57	2.00E+02	1.12E+00	2.67E-01
0.57	3.00E+02	2.66E+00	1.88E-01
0.59	5.00E+01	5.03E-02	7.69E-01
0.59	7.00E+01	1.07E-01	5.95E-01
0.59	1.00E+02	2.42E-01	4.63E-01
0.59	1.50E+02	6.06E-01	3.43E-01
0.59	2.00E+02	1.19E+00	2.84E-01
0.59	3.00E+02	2.88E+00	2.03E-01
0.61	5.00E+01	5.04E-02	7.70E-01
0.61	7.00E+01	1.03E-01	5.73E-01
0.61	1.00E+02	2.47E-01	4.72E-01
0.61	1.50E+02	6.60E-01	3.74E-01
0.61	3.00E+02	3.23E+00	2.28E-01
0.63	5.00E+01	5.04E-02	7.69E-01
0.63	7.00E+01	1.08E-01	6.03E-01
0.63	1.00E+02	2.53E-01	4.82E-01
0.63	2.00E+02	1.44E+00	3.45E-01
0.63	3.00E+02	3.56E+00	2.52E-01
0.65	5.00E+01	5.06E-02	7.73E-01
0.65	7.00E+01	1.10E-01	6.14E-01
0.65	1.00E+02	2.57E-01	4.90E-01
0.65	2.00E+02	1.55E+00	3.71E-01

ContinueTable (B-2). Collected date from the inverted burner

0.65	3.00E+02	3.84E+00	2.72E-01
0.67	5.00E+01	5.11E-02	7.81E-01
0.67	7.00E+01	1.12E-01	6.25E-01
0.67	1.00E+02	2.57E-01	4.91E-01
0.67	2.00E+02	1.69E+00	4.04E-01
0.67	3.00E+02	4.21E+00	2.97E-01
0.69	5.00E+01	5.33E-02	8.15E-01
0.69	7.00E+01	1.15E-01	6.37E-01
0.69	1.00E+02	2.63E-01	5.03E-01
0.69	2.00E+02	1.86E+00	4.44E-01
0.69	3.00E+02	4.66E+00	3.30E-01

Table (B-3). Coating soot particles with DOS

m (fg)	d coated (nm)	d core (nm)	m/m0	d coated/d0	Delta d%	effective density of coated soot (g/cm3)	effective density of core soot (g/cm3)	Shape factor coated	Shape factor core
d fresh=450 nm									
12.6	460.15	462.2	1	1.02	0	0.25	0.24	2.48	2.5
17.5	466.1	456.3	1.39	1.04	1.28	0.33	0.25	1.92	2.46
26.65	426.7	405.1	2.12	0.95	12.35	0.66	0.36	1.3	2.1
37.05	431.4	394	2.94	0.96	14.76	0.88	0.39	1.1	2.03
50.42	465.3	383	4	1.03	17.14	0.96	0.43	1.04	1.95
63.39	500	382.4	5.03	1.11	17.27	0.97	0.43	1.02	1.95
d fresh=350 nm									
6.71	361.5	361.5	1	1	0	0.27	0.27	2.49	2.49
10.59	364.84	349.45	1.58	1.01	3.33	0.42	0.3	1.72	2.38
13.33	353.96	341.02	1.99	0.98	5.67	0.57	0.32	1.41	2.3
20.33	356.5	331.58	3.03	0.99	8.28	0.86	0.35	1.12	2.21
40.53	430.6	314.4	6.04	1.19	13.03	0.97	0.41	1.01	2.06
53.93	477.5	307.8	8.04	1.32	14.85	0.95	0.44	1.01	2
d fresh=150 nm									
1.19	156.3	157.1	1	1	0	0.6	0.59	1.85	1.86
2.37	165	153.4	1.99	1.06	2.36	1.01	0.63	1.1	1.79
7.19	241.8	150	6.04	1.55	4.52	0.97	0.67	1.01	1.73
13.16	305	146.8	11.06	1.95	6.56	0.89	0.72	1.04	1.67
d fresh=100 nm									
0.47	100	103	1	0.97	0	0.9	0.82	1.5	1.58
2	160	100	4.26	1.55	2.91	0.93	0.9	1.06	1.5
3	182	96.7	6.38	1.77	6.12	0.95	0.99	1.02	1.42
4	202	96.8	8.51	1.96	6.02	0.93	0.99	1.02	1.42
5	220	97.15	10.64	2.14	5.68	0.9	0.98	1.03	1.43

Table (B-4) Coating soot particles with Oleic Acid

m (fg)	d coated (nm)	d core (nm)	m/m0	d coated/d0	Delta d %	effective density of coated soot (g/cm3)	effective density of core soot (g/cm3)	Shape factor coated	Shape factor core
d fresh=400 nm									
9.80	416.56	416.56	1.00	1.00	0.00	0.26	0.26	2.47	2.47
20.05	376.00	374.06	2.05	0.90	10.20	0.72	0.36	1.25	2.15
49.06	463.63	343.27	5.01	1.11	17.59	0.94	0.46	1.02	1.91
68.84	526.50	349.70	7.02	1.26	16.05	0.90	0.44	1.03	1.96
96.45	594.50	348.70	9.84	1.43	16.29	0.88	0.44	1.03	1.95
d fresh=350 nm									
7.17	358.00	358.00	1.00	1.00	0.00	0.30	0.30	2.37	2.37
14.45	348.00	336.40	2.02	0.97	6.03	0.65	0.36	1.32	2.18
36.37	416.27	316.30	5.07	1.16	11.65	0.96	0.43	1.01	2.00
51.21	470.00	315.70	7.14	1.31	11.82	0.94	0.44	1.01	2.00
70.29	532.85	308.72	9.80	1.49	13.77	0.89	0.47	1.03	1.94
d fresh=250 nm									
3.51	264.50	264.50	1.00	1.00	0.00	0.36	0.36	2.26	2.26
7.23	259.00	255.00	2.06	0.98	3.59	0.79	0.40	1.22	2.15
17.81	330.00	238.00	5.07	1.25	10.02	0.95	0.5	1.02	1.94
24.86	371.60	239.06	7.08	1.40	9.62	0.93	0.49	1.02	1.95
35.38	420.60	241.60	10.08	1.59	8.66	0.91	0.48	1.02	1.99